



HAL
open science

Study of the bipolar jet of the YSO Th 28 with VLT/SINFONI: Jet morphology and H₂ emission

S.Yu Melnikov, P.A Boley, N.S Nikonova, A Caratti O Garatti, R Garcia Lopez, B Stecklum, J Eislöffel, G Weigelt

► To cite this version:

S.Yu Melnikov, P.A Boley, N.S Nikonova, A Caratti O Garatti, R Garcia Lopez, et al.. Study of the bipolar jet of the YSO Th 28 with VLT/SINFONI: Jet morphology and H₂ emission. *Astronomy and Astrophysics - A&A*, 2023, 673, pp.A156. 10.1051/0004-6361/202140581 . hal-04096370

HAL Id: hal-04096370

<https://hal.science/hal-04096370>

Submitted on 13 Oct 2023









HAL is a multi-disciplinary open access archive for the deposit and dissemination of scientific research documents, whether they are published or not. The documents may come from teaching and research institutions in France or abroad, or from public or private research centers.

L'archive ouverte pluridisciplinaire **HAL**, est destinée au dépôt et à la diffusion de documents scientifiques de niveau recherche, publiés ou non, émanant des établissements d'enseignement et de recherche français ou étrangers, des laboratoires publics ou privés.



Distributed under a Creative Commons Attribution 4.0 International License

Study of the bipolar jet of the YSO Th 28 with VLT/SINFONI: Jet morphology and H₂ emission[★]

S. Melnikov^{1,2} , P. A. Boley^{3,4,★★} , N. S. Nikonova^{4,★★} , A. Caratti o Garatti^{5,6} , R. Garcia Lopez^{6,5} ,
B. Stecklum¹ , J. Eisloffel¹ , and G. Weigelt⁷ 

¹ Thüringer Landessternwarte Tautenburg, Sternwarte 5, 07778 Tautenburg, Germany
e-mail: sme1n2005@gmail.com

² National University of Uzbekistan, Physics Faculty, Department of Astronomy and Atmospheric Physics, 100174 Tashkent, Uzbekistan

³ Visiting astronomer, Laboratoire Lagrange, Université Côte d'Azur, Observatoire de la Côte d'Azur, CNRS, Boulevard de l'Observatoire, CS 34229, 06304 Nice Cedex 4, France

⁴ Moscow Institute of Physics and Technology, 9 Institutskiy per., 141701 Dolgoprudny, Moscow Region, Russia

⁵ INAF – Osservatorio Astronomico di Capodimonte, Salita Moiarriello 16, 80131 Napoli, Italy

⁶ School of Physics, University College Dublin, Belfield, Dublin 4, Ireland

⁷ Max Planck Institute for Radio Astronomy, Auf dem Hügel 69, 53121 Bonn, Germany

Received 16 February 2021 / Accepted 3 March 2023

ABSTRACT

Context. The young stellar object (YSO) Th 28 possesses a highly collimated jet, which clearly exhibits an asymmetric brightness of its jet lobes at optical and near-infrared wavelengths. As with many other YSO outflows, there may be asymmetry in the physical parameters of the jet plasma in opposite jet lobes (e.g. electron density, temperature, and outflow velocity).

Aims. We examined the Th 28 jet at high-spatial resolution in the regions where the jet material is collimated and accelerated. Our goal is to map the morphology and determine its physical parameters. We compared the results with those of other asymmetric YSO jets to determine the physical origin of such asymmetries.

Methods. We used the integral field spectrograph SINFONI on the Very Large Telescope (VLT) of the European Southern Observatory to characterise the jet parameters in a $3'' \times 3''$ field around the central source of Th 28. We present high-resolution spectra of Th 28 covering the *JHK* bands, obtained in June–July 2015.

Results. The images reveal gaseous structures out to distances of a few arcseconds around the stellar jet source. The [Fe II] emission originates in highly collimated jet lobes. Two new axial knots are detected in the bipolar jet, one in each lobe, at angular distances of $1''$ in the blue lobe and $1''.2$ in the red lobe. The H₂ radiation is emitted from an extended region with a radius of $\gtrsim 270$ au, which is perpendicular to the jet. The position–velocity diagrams of the bright H₂ lines reveal faint H₂ emission along both jet lobes as well. The compact and faint H I emission (Pa β and Br γ) comes from two regions, namely from a spherical region around the star and from the jet lobes. The maximum size of the jet launching region is derived as $0''.015$, which corresponds to ~ 3 au at a distance of 185 pc, and the initial opening angle of the Th 28 jet is about 28° , which makes this jet substantially less collimated than most jets from other Classical T Tauri stars (CTTs).

Conclusions. The high-resolution SINFONI images show three groups of lines with different excitation conditions, which trace different gas structures. The emission in [Fe II], H₂, and atomic hydrogen lines suggests a morphology in which the ionised gas in the disc (or at least very close to the jet launching site) appears to be disrupted by the jet. The resolved disc-like H₂ emission most likely arises in the disc atmosphere from shocks caused by a radial uncollimated wind. The asymmetry of the [Fe II] photocentre shifts with respect to the jet source arises in the immediate vicinity of the driving source of Th 28 and suggests that the observed brightness asymmetry is intrinsic as well.

Key words. stars: jets – stars: winds, outflows – stars: variables: T Tauri, Herbig Ae/Be

1. Introduction

Many young stellar objects (YSOs) possess collimated outflows and/or jets, which are believed to allow the removal of excess angular momentum from their accretion discs (Ferreira et al. 2006; Pudritz et al. 2007). However, the complex picture of the transformation of circumstellar accretion into material ejection is not yet fully understood. Various theoretical models assume that the central jet engine should work in both directions in a similar way, producing a symmetrical bipolar jet (e.g. Ferreira & Casse 2004; Meliani et al. 2006; Pudritz et al. 2007). However,

detailed studies have discovered that many of the bipolar YSO outflows exhibit remarkable asymmetries in the physical conditions seen in their opposite lobes on both large and small scales. Not only do some jets have lobes of different brightnesses, they also exhibit different physical parameters of the jet plasma in opposite lobes (e.g. electron density, temperature, radial velocity). For example, Hirth et al. (1994) found that 8 of the 15 bipolar Herbig-Haro (HH) outflows studied show velocity asymmetries between blue and redshifted outflows. Moreover, some objects reveal a single outflow component in only one direction, for example the LkH α 321 jet (Coffey et al. 2004) and HH 34 (Reipurth et al. 2002).

The asymmetry can be intrinsic (i.e. caused by the ‘engine’ itself) or extrinsic (i.e. caused by an inhomogeneous environment). Various mechanisms have been invoked to explain

[★] Based on observations collected at the European Organisation for Astronomical Research in the Southern Hemisphere under ESO program 095.C-0892(A).

^{★★} Former affiliation.

the observed jet asymmetry: variations in the morphology of the magnetic field near the central star (e.g. in HD 163296, Wassell et al. 2006), warped circumstellar discs (e.g. HH 111, Gómez et al. 2013), and interactions between a stellar magnetic field and a circumstellar disc magnetic field (e.g. Matsakos et al. 2012; Dyda et al. 2015). Recent numerical simulations of jets and winds from weakly ionised protoplanetary discs, taking into account non-ideal magnetohydrodynamic effects, also produce asymmetric ejections (cf. Bai 2017; Béthune et al. 2017). The jet appearance is also affected by spatial extinction variations (i.e. extrinsic scenario), in particular shadowing the redshifted part by the disc–envelope. Admittedly, this does not cause differences in the physical parameters; proper extinction correction is provided.

The asymmetric properties of several young T Tauri jets have been analysed using high-resolution observations in recent years. Using high-resolution spectra obtained with the *Hubble* Space Telescope, Melnikov et al. (2009) found that the RW Aur jet has a strong asymmetry in electron density and temperature, excitation, and total hydrogen density between its opposite lobes. At the same time, the jet mass loss rate is similar in the two lobes, as in some other asymmetric jets, for example, DG Tau B (Podio et al. 2011) and HD 163296 (Wassell et al. 2006). Melnikov et al. (2009) concluded that the observed asymmetries of the RW Aur jet can be explained by different environmental conditions around the jet source and not by asymmetric jet formation.

Using high-resolution Echelle spectra obtained with the HIRES spectrograph at the Keck I telescope, Podio et al. (2011) studied the asymmetry of the DG Tau B jet properties, and concluded that it can be caused by a strong interaction of the jet lobes with an asymmetric ambient medium. White et al. (2014) used the near-infrared (NIR) integral-field spectrograph on the Gemini telescope to study the structure of the asymmetric bipolar outflow of DG Tau. They concluded that the approaching jet is propagating in a low-density medium, while the receding jet is colliding with dense material along its path and appears as the large bubble-like structure visible in [Fe II] 1.64 μm at 200 au from the source. White et al. (2014) interpreted the properties of the observed H₂ emission as evidence for a clumpy medium above the circumstellar disc, which interacts with both the jet and the gaseous bubble. Finally, they concluded that the bipolar outflow from DG Tau is intrinsically symmetric, but the observed asymmetries are caused by an asymmetric distribution of the ambient circumstellar material. Three YSO jets have been studied during the last decade, RW Aur, DG Tau, and DG Tau B, which are visually asymmetric but seem to have intrinsic symmetry.

For this paper, we used the high resolution integral field spectrograph VLT/SINFONI to study another asymmetric bipolar microjet from the YSO ThA 15-28 (V1190 Sco, Sz 102, hereafter Th 28) within 3'' of the central source. Th 28 (age $\sim 1\text{--}2$ Myr, Comerón & Fernández 2010) is located in the Lupus 3 cloud, at a distance of ~ 185 pc¹ (Galli et al. 2013). The bipolar jet from Th 28, first discovered by Krautter (1986), exhibits a noticeable brightness asymmetry of its lobes, visible,

¹ A much larger distance is suggested by the calibration of Bailer-Jones et al. (2018) based on *Gaia* DR2 (Gaia Collaboration 2018) parallax measurements, resulting in an estimated distance of 462^{+278}_{-126} pc. However, because Th 28 is not a point source at optical wavelengths, this estimate may not be reliable. In *Gaia* DR3 (Bailer-Jones et al. 2021) the fidelity value for Th 28 is ~ 0.05 , whereas any parallaxes with a fidelity value of ≥ 0.5 are considered reliable. This confirms that the *Gaia* parallax for Th 28 is not trustworthy.

for example, in [S II] lines (Wang & Henning 2009). This collimated jet can be traced up to distances of several dozen arcseconds, with a few bow shocks visible along the jet axis on both sides of the source (Wang & Henning 2009; Murphy et al. 2021). The overall position angle (PA) of the flow is almost east–west, with the brighter red lobe of the microjet pointing towards the west. In a recent ALMA study, Louvet et al. (2016) mapped the CO lines in Th 28, and found a lower limit for the inclination of the disc rotation axis to the line of sight of $i > 73^\circ$, and a jet inclination of 82° . This confirmed the previous conclusion of Krautter (1986) that the global inclination of the jet seems close to the plane of the sky ($i \sim 82^\circ$). Murphy et al. (2021) found that the inclination of the two jet lobes is different: $i_{\text{red}} = 83.5^\circ$, whereas $i_{\text{blue}} = 77^\circ$. Th 28 is also known as a source of X-ray emission (Gondoin 2006). Using the adaptive optics (AO) correction of the SINFONI integral field spectrograph, our objective was to obtain a spatial resolution ~ 3 times higher than that achieved with the ISAAC slit spectrograph (0''.5) by Coffey et al. (2010). In addition, the integral-field observations provide us with the opportunity to study the distribution of the emitting gas using spectroastrometric analysis.

The work is organised as follows. Details of SINFONI observations and data reduction are described in Sect. 2. In Sect. 3 we represent the main results of the analysis of the observations. In Sect. 3.1 we consider the general morphology of the Th 28 jet formation region, based on the analysis of different NIR (1.10–2.45 μm) spectral lines. In Sect. 3.2 we discuss the gas kinematics from an analysis of the [Fe II] lines. In Sect. 3.3 we analyse the extinction A_V calculated from the [Fe II] line flux ratios. In particular, in Sect. 3.4 we perform a spectroastrometric analysis and compute the photocentre shifts of the [Fe II], Pa β , Br γ , and H₂ lines with respect to the central source. In Sect. 3.5 we analyse the morphology of the region that emits in the H₂ lines and present the physical parameters derived from the analysis of these molecular lines (Sect. 3.6). In Sect. 4 we report our spectral analysis of the jet and discuss our results. In Sect. 5 we summarise our findings and the scenario adopted for the jet.

2. Observations and data analysis

Th 28 (RA = 16^h 08^m 30^s Dec = $-39^\circ 03' 11''$) was observed with the SINFONI instrument at the VLT-UT4 telescope (ESO, Paranal, Chile) on June 4, 2015 (*J*, *K*), and July 17, 2015 (*H*). SINFONI is a NIR integral field spectrograph that works in combination with adaptive optics (Eisenhauer et al. 2003); it was developed for observations of single faint objects. The Integral Field Unit (IFU) was used to obtain two-dimensional (2D) spectroscopy of the Th 28 jet in the wavelength bands *J*, *H*, and *K*, which provided spectral resolutions of $R = 2000$ (150 km s⁻¹), 3000 (100 km s⁻¹), and 4000 (75 km s⁻¹), respectively. The wavelength ranges of the filters, excluding edge effects, are 1.10–1.40 μm for *J*, 1.45–1.85 μm for *H*, and 1.95–2.45 μm for *K*. The field of view (FoV) with adaptive optics (AO) mode is $3'' \times 3''$ with a spaxel size of $0''.05 \times 0''.1$, where the detector direction corresponding to the larger pixel size was aligned with the jet axis of Th 28. The pipeline reduction rescales the cubes so that the final reduced cubes have pixels of the same size (0''.05) for both the *X*- and *Y*-directions. Since Th 28 is quite bright ($R = 15.4$ mag), it was used as a natural guide star for the AO system. A total integration time of 30 min per band was used. The seeing conditions during July 17 (DIMM = 0''.6 for *H* observations) were approximately twice better than during June 4 (DIMM $\approx 1''.25$ for *J* and *K* observations). The angular sizes of the central emission region in Th 28, derived from the continuum

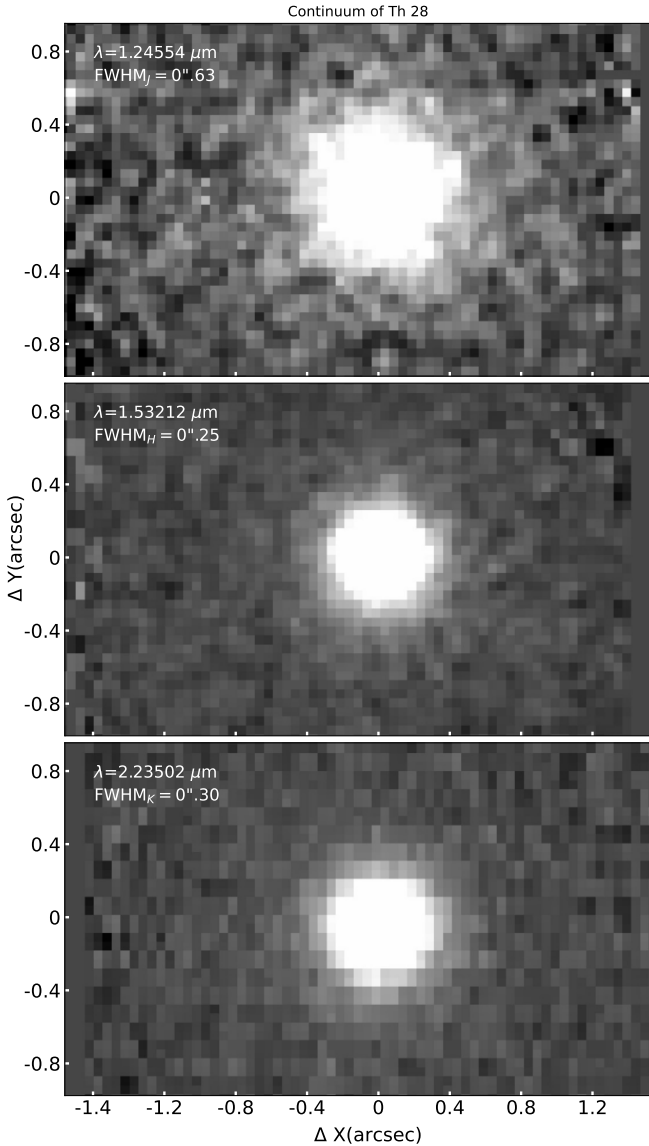


Fig. 1. Continuum images of Th 28 at the *J*, *H*, and *K* band centres, with corresponding measured FWHMs of the continuum emission.

emission, amount to $FWHM_J \approx 0''.63$, $FWHM_H \approx 0''.23$, and $FWHM_K \approx 0''.31$ (single frames with continuum images are shown in Fig. 1). The position angle (PA) of the SINFONI instrument was aligned with the jet PA (98°) so that the *Y*-direction in the observed frames coincides with the jet axis. To perform an absolute flux calibration, we observed the solar-type spectrophotometric standard HD 154504. Several telluric standards (HIP 080405, 082430, 090361) were also measured for atmospheric telluric correction.

The SINFONI integral-field spectroscopic observations produce raw science frames that carry both spatial and spectral information. Basic reduction of raw science images was performed according to the SINFONI standard data reduction recipes (Modigliani et al. 2007), which include bad pixel removal, flat field, and dark correction. As a result, the frames were reconstructed as a 3D data cube, where every position in the $3'' \times 3''$ field has a spectrum with a step of 2.5 \AA ($0.00025 \mu\text{m}$).

The wavelength calibration based on observations of a xenon–argon arc lamp led to high systematic errors. Therefore, for this purpose we used telluric lines, which provide a better

calibration accuracy (e.g. Agra-Amboage et al. 2014). The estimated uncertainties of the measured wavelengths after using the telluric lines are $\sim 0.1\text{--}0.3 \text{ \AA}$ (ranging between $\pm 1\text{--}10 \text{ km s}^{-1}$, depending on the wavelength). The estimated FWHM of the telluric lines at *J*, *H*, and *K* are 205 ± 33 , 155 ± 16 , and $139 \pm 30 \text{ km s}^{-1}$, respectively. All radial velocities are systemic and measured with respect to the local standard of rest (LSR; $V_{\text{LSR}} = 3 \text{ km s}^{-1}$), which was obtained from recent ALMA observations by Louvet et al. (2016). Absolute flux calibration was performed by measuring the density flux (in counts) on the standard star by fitting a 2D Gaussian profile at each wavelength. The detector count rates were then converted to $\text{erg s}^{-1} \text{ cm}^{-2} \mu\text{m}^{-1}$ by comparison with the reference spectrum of the spectral standard. Telluric standard stars were used to correct the spectrum for the detector spectral response. Standard–telluric stars and the science target were observed at similar airmasses, so no atmospheric extinction corrections were applied. Finally, we subtracted the continuum emission (a combination of stellar, dust, and scattered emission) at each position in the field by fitting a third-order polynomial to the continuum at each point.

3. Results

We inspected the data cubes and identified all emission features found in the *J*, *H*, and *K* bands (see Table 1). The average 1D spectra in the central $0''.5 \times 0''.5$ region are shown in Fig. 2, where the identified emission lines are marked. These emission lines represent three main groups: forbidden [Fe II] lines, molecular hydrogen lines (H_2), and atomic hydrogen lines. Atomic H lines are mostly represented by Brackett-series recombination lines. The *K* band contains faint Br γ emission, and the lines from Br $_{10}$ to Br $_{16}$ are also detected in the *H* band; Br δ and Br $_{9}$ are not detected as they fall into the wavelength gap between the *H* and *K* bands. In the *J* band, the Pa β line is detected. The brightest H_2 lines are found in the *K* band, but some molecular hydrogen emission is also detected in the *H* band. Two emission lines that do not belong to these large groups were identified as [P II] $1.1886 \mu\text{m}$ and He I $2.0605 \mu\text{m}$, which were also detected in the spectrum of the YSO jet HH 99B (Giannini et al. 2008). The vacuum wavelengths of the identified lines are listed in Table 1, and the origin of the line is identified based on their morphology.

3.1. Jet morphology in atomic lines in the $3'' \times 3''$ region

Figure 3 shows the total flux maps of the brightest emission lines, which trace different gaseous structures in the vicinity of Th 28. First, we note that the bright [Fe II] emission ([Fe II] 1.257 , 1.534 , $1.644 \mu\text{m}$) seems to originate in the jet lobes, since its elongation coincides with the jet axis. With the PA = 98° used for SINFONI, the upper jet lobe in Fig. 3 corresponds to the blueshifted (east) lobe, while the lower lobe (i.e. the brightest jet component) corresponds to the redshifted component (west). The maps also indicate that the [Fe II] emission has the same asymmetric shape between the red and blue lobes as seen in the [S II] lines (Coffey et al. 2010; Wang & Henning 2009). However, the fainter [Fe II] $1.295 \mu\text{m}$ (*J* band) is rounder and is reminiscent of the shape of Pa β . At the same time, although the shape of the bright [Fe II] $1.257 \mu\text{m}$ emission is wider than the [Fe II] lines in the *H* band (obtained with better seeing), it still traces the shape of the jet. Therefore, the [Fe II] $1.295 \mu\text{m}$ line seems also to originate in the jet, but its emission is bright enough for detection only in the immediate vicinity of the jet source. The bright [Fe II] lines show two knots at similar distances in opposite directions. Almost all bright iron lines in the redshifted lobe

Table 1. Emission lines detected in SINFONI *JHK* bands.

Element	λ_{vac} (μm)	Flux ^(*) ($\times 10^{-16}$)	Origin	Element	λ_{vac} (μm)	Flux ^(*) ($\times 10^{-16}$)	Origin	Element	λ_{vac} (μm)	Flux ^(*) ($\times 10^{-16}$)	Origin
<i>J</i> -band				[Fe II]	1.5999	41.33 \pm 0.13	Jet	<i>K</i> -band			
				Br ₁₃	1.6119	1.65 \pm 0.03		H ₂ 1-0 S(3)	1.9576	103.66 \pm 0.29	Disc
[P II]	1.1886	6.97 \pm 0.04	Disc?	Br ₁₂	1.6416	3.24 \pm 0.04		H ₂ 1-0 S(2)	2.0338	21.28 \pm 0.08	Disc
[Fe II]	1.2492	0.40 \pm 0.02		[Fe II]	1.6440	243.30 \pm 0.41	Jet	[Fe II]	2.0468	5.04 \pm 0.03	
[Fe II]	1.2570	296.58 \pm 0.29	Jet	[Fe II]	1.6642	20.28 \pm 0.08	Jet	He I	2.0605	1.47 \pm 0.01	
[Fe II]	1.2708	16.72 \pm 0.07		[Fe II]	1.6773	43.20 \pm 0.13	Jet	H ₂ 1-0 S(1)	2.1218	76.14 \pm 0.22	Disc
[Fe II]	1.2791	37.36 \pm 0.08	Jet?	Br ₁₁	1.6817	7.83 \pm 0.08		[Fe II]	2.1338	1.73 \pm 0.02	
Pa β	1.2822	146.84 \pm 0.23	Disc+jet	H ₂ 1-0 S(9)	1.6877	2.48 \pm 0.03		Bry	2.1661	8.57 \pm 0.14	Disc+jet?
[Fe II]	1.2946	48.55 \pm 0.09	Jet?	[Fe II]	1.7116	6.15 \pm 0.05	Jet	H ₂ 1-0 S(0)	2.2233	12.66 \pm 0.05	Disc
[Fe II]	1.2985	9.15 \pm 0.04		H ₂ 1-0 S(8)	1.7147	0.33 \pm 0.01		[Fe II]	2.2244	7.51 \pm 0.04	Jet
[Fe II]	1.3209	72.29 \pm 0.10	Jet	Br ₁₀	1.7371	6.39 \pm 0.07		H ₂ 2-1 S(1)	2.2477	0.71 \pm 0.01	
[Fe II]	1.3284	21.15 \pm 0.06		[Fe II]	1.7454	8.98 \pm 0.06	Jet	H ₂ 1-0 Q(1)	2.4066	89.31 \pm 0.26	Disc
<i>H</i> -band				[Fe II]	1.7480	7.71 \pm 0.04	Disc	H ₂ 1-0 Q(2)	2.4134	9.70 \pm 0.04	Disc
[Fe II]	1.5339	60.74 \pm 0.20	Jet	[Fe II]	1.7489	1.13 \pm 0.01	Jet	H ₂ 1-0 Q(3)	2.4237	56.65 \pm 0.18	Disc
Br ₁₇	1.5443	0.31 \pm 0.15		H ₂ 1-0 S(6)	1.7879	1.36 \pm 0.06		H ₂ 1-0 Q(4)	2.4375	3.74 \pm 0.08	Disc
Br ₁₆	1.5562	0.81 \pm 0.02		[Fe II]	1.7976	16.30 \pm 0.08	Jet				
Br ₁₄	1.5885	1.52 \pm 0.03		[Fe II]	1.8005	17.29 \pm 0.10	Jet				
				[Fe II]	1.8099	35.50 \pm 0.12	Jet				

Notes. (*) The flux is integrated over the continuum-subtracted spectrum and in $\text{erg s}^{-1} \text{cm}^{-2}$ units. For the H₂ lines the flux is summed for the bright central core with a size of $\sim 1''.5$ and does not include the faint periphery. For [Fe II] lines the bright areas of emission with $S/N > 3$ are integrated along the jet lobes.

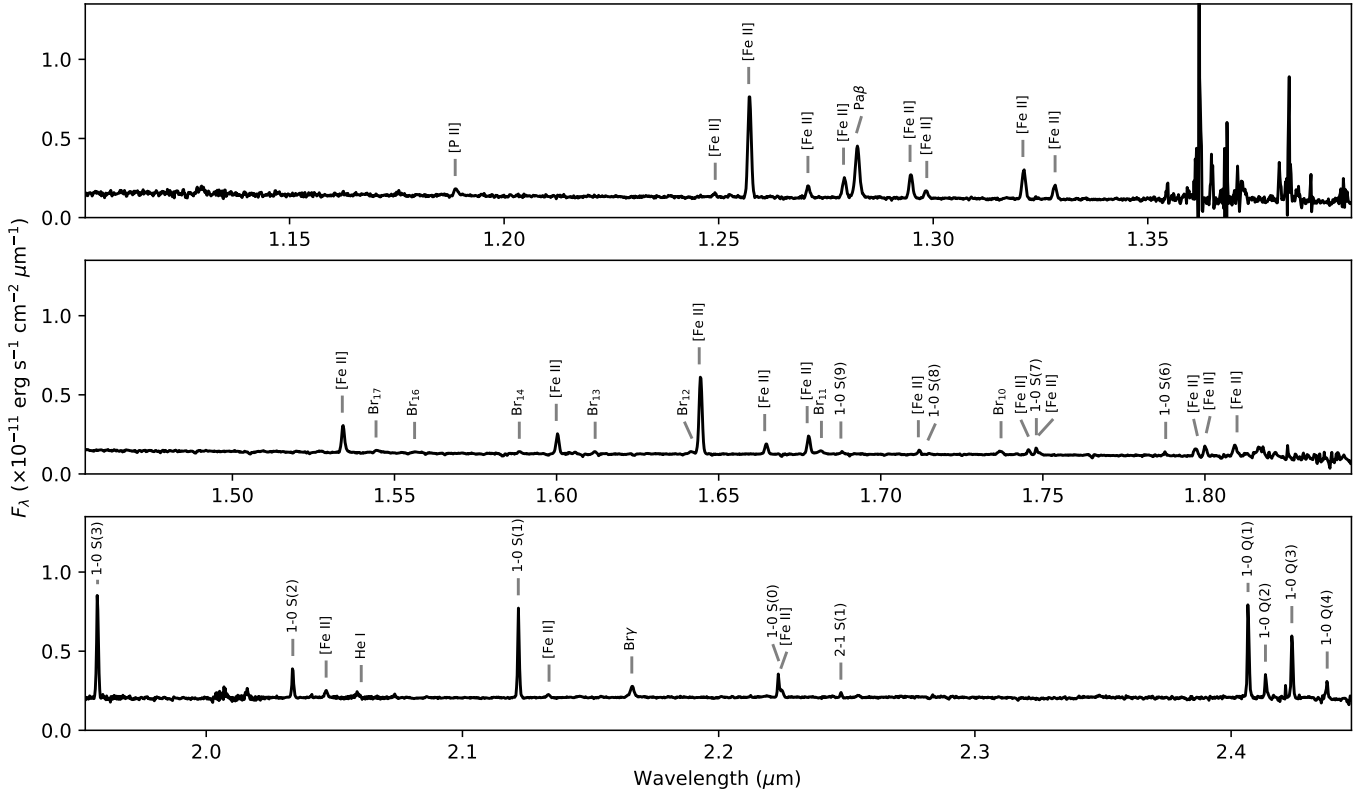


Fig. 2. 1D spectra in the *J*, *H*, and *K* bands, summed over the central $0''.5 \times 0''.5$ of Th 28.

show an emission knot at $1''.2$ from the central source, while the brightest [Fe II] 1.644 μm line reveals a faint knot at $1''$ in the blueshifted beam (Figs. 3 and 4).

Unlike the [Fe II] lines, both the Pa β and Bry emitting regions are mostly round and symmetric, with brightness maxima roughly coincident with the position of the stellar continuum. Measurement of the continuum-subtracted emission region shows that the Pa β line is much brighter and more

extended than the Bry line. We performed Moffat fitting of the 1D profiles along the jet axis (*Y*-direction) and perpendicularly to this direction (*X*-direction) to determine if there is any departure of the Pa β - and Bry-emitting regions from a circular shape. The fit of the Pa β line intensity distribution shows that it is generally somewhat round ($FWHM_X = 0''.66 \pm 0''.03$, $FWHM_Y = 0''.70 \pm 0''.04$), while the angular size of the Bry emitting region is $FWHM_X = FWHM_Y = 0''.33 \pm 0''.01$.

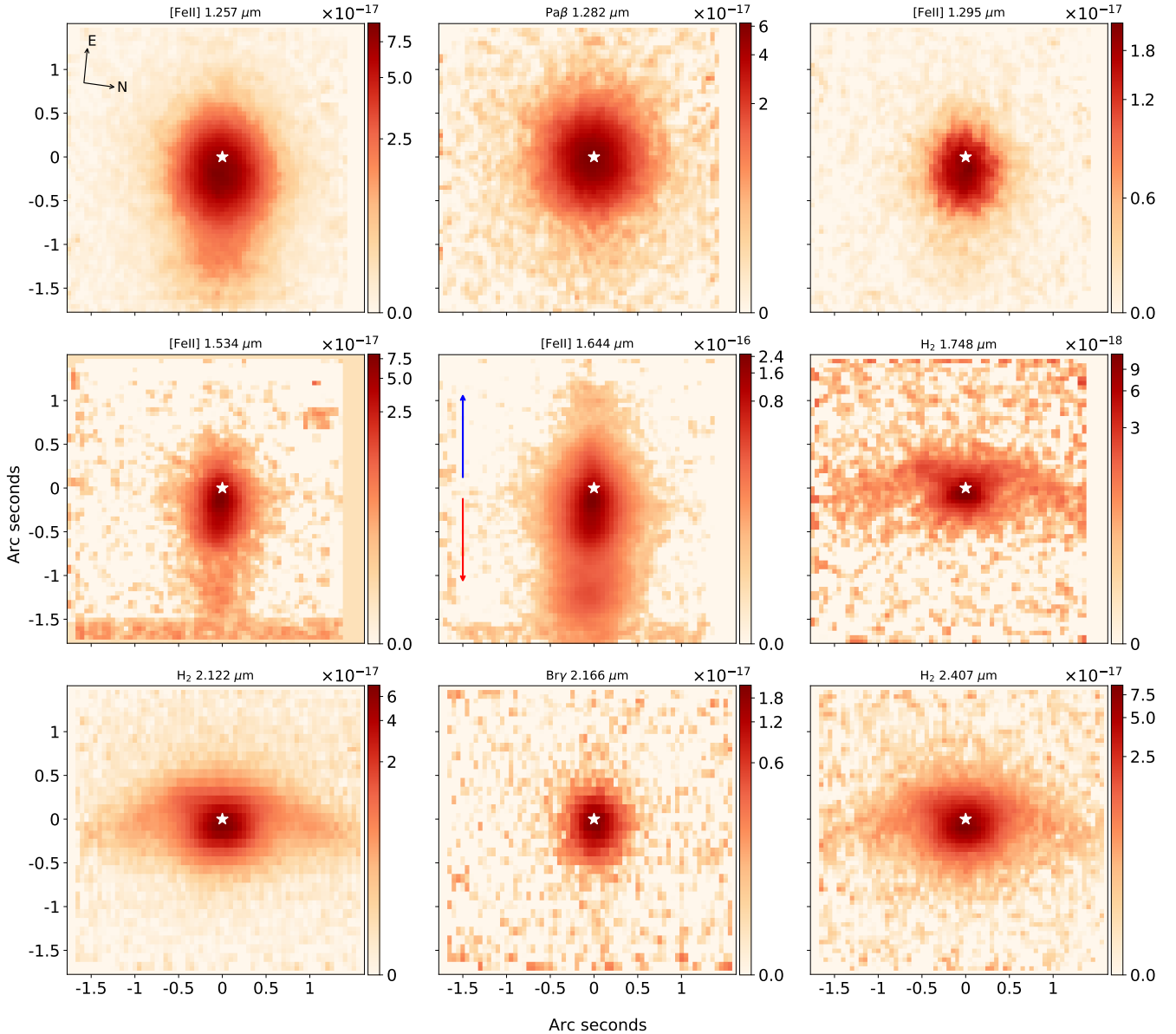


Fig. 3. Total line flux maps of the nine brightest emission lines in Th 28 over the *J*, *H*, and *K* bands. Each map shows the total line flux integrated over all the velocity frames where emission is detected. The star gives the position of the central source, calculated from the continuum (stellar) profile. The coloured arrows indicate the direction of the blue and red lobes. The vertical log-scale shows the fluxes in $\text{erg s}^{-1} \text{cm}^{-2}$.

We compared these values with the FWHM of the continuum profiles to check whether the HI emitting regions are spatially resolved. For this goal, we computed the averaged continuum FWHM from 15 single frames from both sides of both lines (in total, 30 frames for each line). The distribution of these FWHM values is flat and does not show any wavelength dependence for these spectral regions. We performed a Moffat 1D fitting of the stellar profile of the continuum and found that for the Pa β region, the continuum has a similar angular size (i.e. $FWHM_X = 0''.67 \pm 0''.05$ and $FWHM_Y = 0''.69 \pm 0''.05$). For the Bry region, the fitted continuum profile had $FWHM_X = 0''.33 \pm 0''.01$ and $FWHM_Y = 0''.32 \pm 0''.01$. Therefore, the results imply that both the Pa β - and Bry-emitting regions are not resolved. This agrees with the results of Caratti o Garatti et al. (2016) for the massive YSO IRAS 13481-6124 (also with a jet), where the Bry-emitting region is very compact. However, Caratti o Garatti et al. (2016) used interferometric techniques

and concluded that the Bry region is extended, tracing a jet-like structure.

At the same time, Fig. 3 shows very faint emission along the jet lobes in both Bry and Pa β . The position–velocity (PV) diagram of the Pa β line from Coffey et al. (2010) also confirms that some part of this emission can come from the jet beam, primarily from the redshifted lobe. We calculated a PV diagram of Pa β for the SINFONI data and also found that both jet lobes show faint emission in this line. Our results also indicate that the red Pa β lobe is brighter than the blue one, which agrees with Coffey et al. (2010). The 1D fitting of the Pa β and Bry integral spectra shows that the two lines have similar and wide profiles, with $FWHM_{in}(\text{Bry}) = 225 \text{ km s}^{-1}$ and $FWHM_{in}(\text{Pa}\beta) = 220 \text{ km s}^{-1}$. Both lines are redshifted with respect to the system velocity, but the peak of the Bry emission is at $+18 \pm 4 \text{ km s}^{-1}$, whereas the peak of the Pa β emission is at $+34 \pm 3 \text{ km s}^{-1}$. These results agree with the peak radial velocities (RVs) derived by

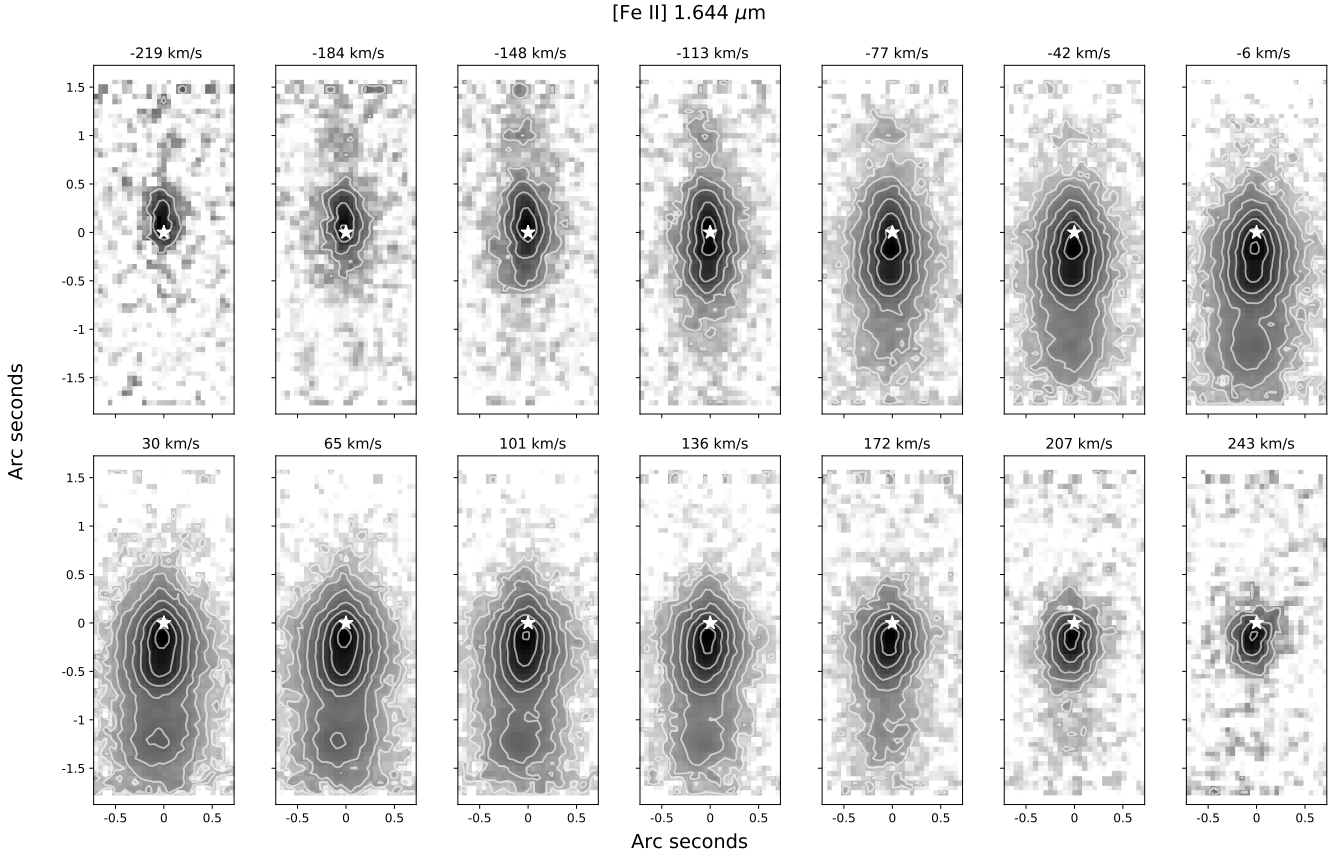


Fig. 4. Continuum-subtracted channel maps for [Fe II] 1.644 μm . The 14 panels show that the [Fe II] emission covers a wavelength range from -220 km s^{-1} to 243 km s^{-1} . The peak position of the continuum flux is indicated by a white star. Contours in units of $\text{erg s}^{-1} \text{ cm}^{-2} \mu\text{m}^{-1}$ consist of nine levels from 2×10^{-15} to 3.2×10^{-13} .

Coffey et al. (2010) for the slit parallel to the jet axis for Pa β and Br γ in the red lobe.

We show the composite image of Th 28 of three bright emission lines, Pa β , [Fe II] 1.644 μm , and H $_2$ 2.122 μm , in Fig. 5. The fluxes of all the lines were integrated over all velocity bins with line emission. Three differently coloured small squares give the position of the continuum stellar profile near each line and perfectly match within the uncertainties. As can be seen, the plane of the disc-like emitting H $_2$ area is orthogonal to the jet axis. The faint emission knot in [Fe II] in the upper (blueshifted) jet lobe is also visible in the combined image.

3.2. Jet kinematics

Figure 4 shows the velocity channel maps, with the radial velocity distribution of continuum-subtracted [Fe II] emission from the 1.644 μm line. The 14 frames clearly exhibit a complex behaviour of gas emission in both the red- and blueshifted jet lobes. First, the gas has an asymmetrical velocity distribution. The RV extends up to -220 km s^{-1} in the blueshifted lobe, while in the redshifted lobe it is more extended and reaches up to 243 km s^{-1} . Interestingly, the redshifted jet lobe becomes visible at negative RVs (i.e. the bipolar jet looks nearly symmetrical at $\text{RV} = -113 \text{ km s}^{-1}$). The same effect can also be seen in the opposite direction: emission from the blueshifted lobe is still detectable at redshifted velocities (within $0''.5$ of the central source). Since the jet is located near the plane of the sky, this behaviour implies that we register the reverse velocity components of the emission, which can form, for instance, from divergent flows if the jet open-

ing angle is larger than the inclination of the jet to the sky plane. Another source of the reversal components could be the possible contribution from scattering radiation by the gas–dust structures of the jet. The FWHM of the instrumental spectral profile in the H band is $\sim 110 \text{ km s}^{-1}$ and is spread over three to four channel maps, spaced by 36 km s^{-1} . This also influences the appearance of the radiation from the outer line wings. The emission maps also show a displacement of the photocentre with respect to the stellar position, which is discussed in Sect. 3.4.

To calculate the maximum RVs of the jet material, we constructed a PV diagram for the [Fe II] 1.644 μm line (Fig. 6). The distributions of RV_{peak} and FWHM_{in} derived from fitting the PV diagram are shown as a function of distance from the source. The figure also shows the spectral profiles derived at selected positions and a fit of the line profiles using a Moffat function. The fitting shows that the kinematics of the [Fe II] emission along the entire redshifted lobe is quite stable, with a peak velocity of $+44 \pm 7.7 \text{ km s}^{-1}$ at a distance of $1''.7$. However, the blue jet has a different morphology and the peak blueshifted velocities are not as evident or as stable as those of the redshifted velocities. Our fitting shows that the RVs gradually increase from low values at the positions closest to the central source to high absolute values at far distances, even exceeding the velocities derived in the receding lobe. For positions up to $+0''.5$, the peak RVs do not exceed -20 km s^{-1} . For example, $\text{RV}_{\text{peak}} = -14 \text{ km s}^{-1}$ at $\Delta Y = +0''.4$ (Fig. 6), but at greater distances ($>+0''.5$) the gas in the approaching lobe reaches large negative RVs. The panel for $\delta = +1''.0$ in Fig. 6 shows the emission line profile in the faint blueshifted knot, and was summed over 3 pixels, with an

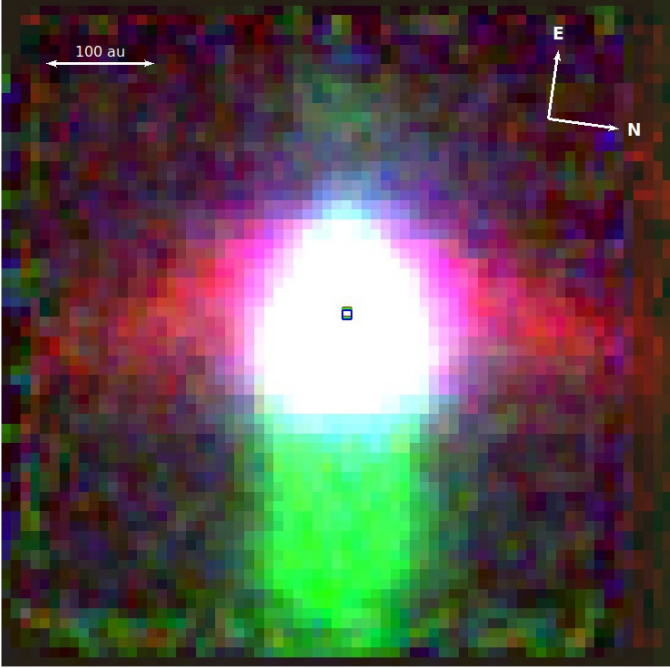


Fig. 5. Tricolour map of the $3'' \times 3''$ field around Th 28, combined from three emission lines outlining different emission regions: blue ($\text{Pa}\beta$), green ([Fe II] 1.644 μm), and red (H_2 2.122 μm). The plane of H_2 -emitting gas is clearly orthogonal to the position of jet axis outlined by forbidden [Fe II]-emission. Three small squares give the position of the star calculated from the continuum stellar profile.

average distance from the central source of $1''.0$. The peak RV in the knot is $\sim -100 \text{ km s}^{-1}$ (i.e. twice as large as in the opposite direction). For the blue lobe, the derived $FWHM_{\text{in}}$ varies from large values ($\sim 270 \text{ km s}^{-1}$) close to the source to $\sim 80 \text{ km s}^{-1}$ at the most distant measured positions. This also differs from the FWHM distribution in the red lobe, where the FWHMs of [Fe II] 1.644 μm are similar and range between 90 and 150 km s^{-1} for all positions along the red lobe. The $FWHM_{\text{in}}$ measured at the source position corresponds to 170 km s^{-1} .

3.3. Determination of A_V from [Fe II] lines

The [Fe II] lines from the same upper excitation state are often used to determine the visual extinction A_V . Their intrinsic ratios are determined by the Einstein A coefficient (which corresponds to the case of $A_V = 0$) and are not affected by the physical conditions in the gas plasma. We used the [Fe II] 1.644, 1.321, and 1.257 μm lines to determine A_V as they all form with an upper level of $a^4\text{D}_{7/2}$ and are bright in the Th 28 spectra. The intrinsic [Fe II] 1.644/1.257 and 1.644/1.321 ratios, derived from the Einstein A coefficient, correspond to 0.88 and 3.13 (Smith & Hartigan 2006), respectively. To calculate A_V from the line ratio, we used the extinction law of Cardelli et al. (1989).

In our case, however, the [Fe II] 1.644 and 1.257 μm lines were obtained under different observation conditions, and the observed ratio appears to be affected by different seeing. To eliminate problems due to different seeing and PSF, we integrated the flux of these [Fe II] lines across the width of the jet and calculated the [Fe II] 1.644/1.257 ratio along the jet (Fig. 7). The obtained ratios (within the estimated errors) were mostly lower than the intrinsic ratio of Smith & Hartigan (2006), and there are a few positions near the jet source in the red lobe where this line ratio is higher than the intrinsic one, 1.05 ± 0.05 which corresponds to

$A_V \approx 2$. We also note that the [Fe II] 1.644/1.257 value averaged over the entire jet beam is 0.72 ± 0.02 , which is consistent within the errors with that of the P Cygni nebula for $A_V = 0$ calculated using the Einstein A coefficient from Nussbaumer & Storey (1988) (Smith & Hartigan 2006). Unfortunately, there is a large uncertainty in determining the Einstein A coefficient, which reaches more than 30% by computing them with different methods (Giannini et al. 2008). Recently, Giannini et al. (2015) performed an empirical determination of the intrinsic ratios of several strong [Fe II] lines in the spectrum of the bright HH object HH 1. They found that the ratios agree better with the predictions of the relativistic Hartree-Fock model of Quinet et al. (1996). However, our observed [Fe II] 1.644/1.257 ratio is lower than those determined for HH 1 for the $A_V = 0$ case at many of these positions along the Th 28 jet.

To calculate the [Fe II] 1.644/1.321 ratio (Fig. 7), we again used the [Fe II] fluxes integrated perpendicularly across the jet and calculated the ratio along the jet lobes. The ratio values are above the intrinsic ratios in the red lobe at the two sections, between -0.5 and 0 arcsec and between -1.6 and -0.85 . Although different authors (Nisini et al. 2005; Podio et al. 2006) point out that the [Fe II] 1.644/1.257 ratio overestimates A_V compared to that calculated with [Fe II] 1.644/1.317, the two ratios give almost the same $A_V \approx 2''$ between -0.5 and 0 arcsec (the red lobe). However, [Fe II] 1.644/1.317 between -1.6 and -0.85 gives much higher ratios that allow us to calculate $A_V = 5'' - 6''$, which is higher than that measured at $-0.5 - 0$ arcs. This is unusual, however, some scattering of the [Fe II] emission in the central regions which could artificially lower the estimate of A_V in the regions closer to the source is possible. We also note that from -1.6 to -0.85 arcsec the flux ratios have higher errors than near the jet source. In any case, the $A_V = 2'' - 6''$ values measured from the two [Fe II] ratios are similar to those estimated from H_2 ($A_V = 1'' - 6''$).

Although the [Fe II] 1.644/1.257 ratio is mostly lower than the intrinsic ratio, we note that the behaviour of the two ratios correlates throughout the jet. For example, both ratios show local maxima at $1''$, which roughly coincides with the position of the knots in each lobe. It is especially prominent in the [Fe II] ratios between -1.6 and -0.85 arcsec. The lack of reliable values for A_V in the blue lobe probably means a lower extinction here compared to the red lobe. We also compared the results with the models of Hartigan et al. (2004), which predict the flux ratios of some bright [Fe II] lines. For example, the models for [Fe II] 1.644/1.257 and 1.644/1.321 give the same ratio values of 0.96 and 3.70 for all models considered in that work. However, our derived [Fe II] 1.644/1.257 and 1.644/1.321 ratios are also mostly lower than those predicted by Hartigan models.

3.4. Emission photocentre shifts

To study the gas extension and shape of the emitting region, we analysed the position of the emission photocentre with respect to the stellar continuum. First, Fig. 3 (and Fig. 4) reveals a clear displacement of the maximum of [Fe II] emission, relative to the stellar position, directly from the observed maps.

To extract the exact XY positions, namely orthogonal and along the jet axis, of the line emission maxima and those of the continuum centre, we used a 2D Moffat fitting, which shows smaller residuals than the 2D Gaussian fitting. To calculate the relative position of the photocentre and avoid an incorrect displacement of gaseous emission with respect to stellar position because of problems with continuum subtraction, we fitted the gaseous emission plus the continuum for these lines. We

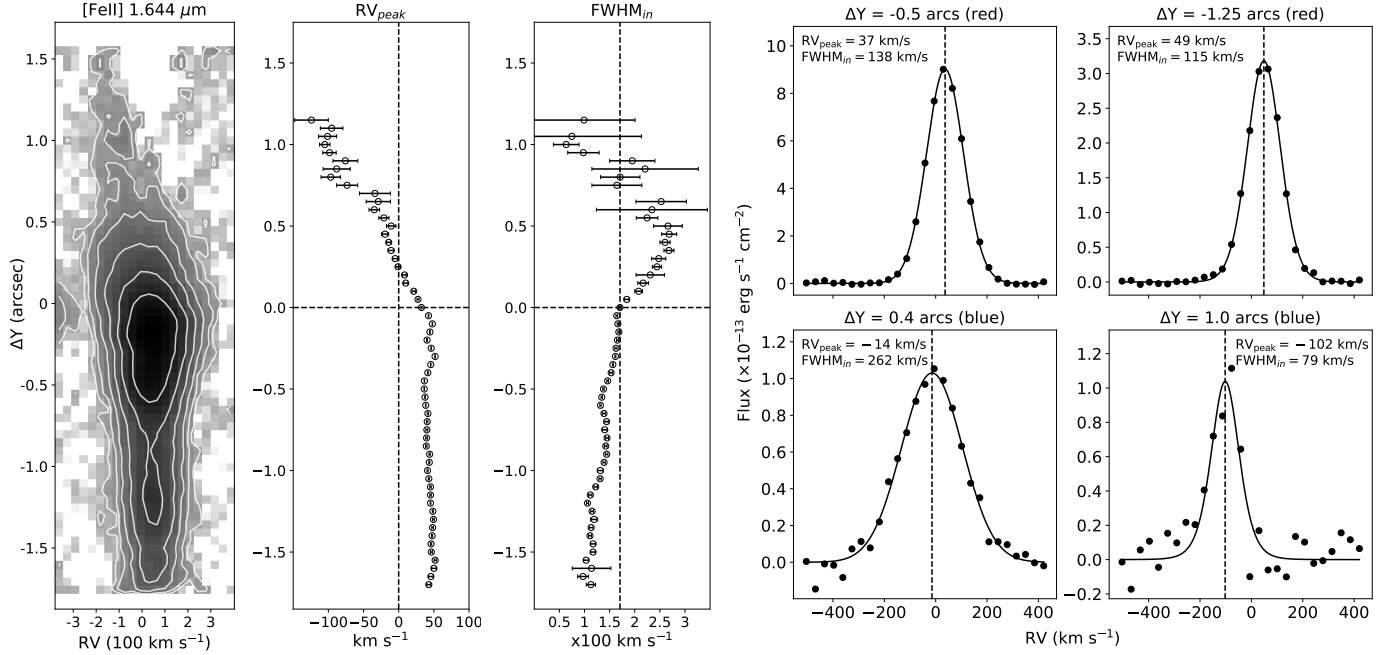


Fig. 6. Distribution of the [Fe II] 1.644 μm emission along the jet. Left image: PV diagrams of [Fe II] 1.644 μm line in the Th 28 jet, obtained by coadding fluxes in the 16 spectral frames across the jet. Logarithmic contours are drawn from 10^{-14} $\text{erg s}^{-1} \text{cm}^{-2} \text{arcsec}^{-2} \text{\AA}^{-1}$, with an incremental logarithmic step of 0.3 dex. Two central panels: RV_{peak} and $FWHM_{\text{in}}$ derived from fitting the PV diagram as a function of the distance from the source. The vertical line in the FWHM panel corresponds to 170 km s^{-1} measured for the position of the source. Right four panels: Spectral profiles across the jet at selected position in the blue and red lobes (black points). The data was fit using a Moffat function (solid line). The intrinsic FWHM and the peak RV are shown at the top of each panel.

corrected the derived displacement for the line-to-continuum ratio. Since the signal from the line approaches zero in the wings, the noise (and hence a measured error of the signal) increases exponentially. The effects of background noise can also be considerable; to account for this, we applied a correction to those positions in the line cores where the detection of the line signal was reliable ($S/N > 0.1$; see Fig. 9) and the background noise was low. The derived errors are shown only for these positions. Figure 8 shows how the position of the photocenter changes for several bright lines that trace different gaseous structures: [Fe II] 1.534, 1.644 μm , Pa β , Bry, and H₂ 2.122, 2.406 μm . To verify these results, we repeated the Gaussian fitting on images with the pure emission after the stellar continuum subtraction. The second method showed that all of the emission lines exhibit a photocentre shift with amplitudes similar to those found in the case of the line plus continuum images.

Our calculated XY distribution of the maximum [Fe II] emission as a function of wavelength (Fig. 8) reveals that the shift of the forbidden emission with respect to the continuum position follows the jet beams, which the emission traces (i.e. for the blueshifted lobe) and the photocentre shifts to the same direction, while for the redshifted lobe the photocentre shifts along the red lobe direction. Furthermore, the photocentre shift along Y in the redshifted lobe is larger than in the blueshifted direction. This behaviour correlates with the brightness asymmetry of the jet lobes. Our measurements show that the [Fe II] line at 1.644 μm , formed with an upper level ($a^4D_{7/2}$), and [Fe II] 1.279 μm line, formed with $a^4D_{3/2}$, reveal similar photocentre shifts in the red lobe ($0''.31$ and $0''.28$, respectively). At the same time, the [Fe II] 1.534 μm lines formed with $a^4D_{5/2}$ are displaced by a smaller distance ($0''.18$). At the adopted distance for Th 28 of 185 pc, this means that the [Fe II] emission with different excitation reaches its maximum at different distances: ~ 55 and

~ 33 au from the central star, respectively. At the same time, the strong [Fe II] 1.534 and 1.644 μm lines exhibit a photocentre shift of $0''.01$ – $0''.05$ for the blueshifted lobe. The strongest line, [Fe II] 1.257 μm , has the strongest shift in the Y -direction ($0''.14$).

Unlike the [Fe II] lines, the emission regions of Pa β and Bry, as well as the H₂ lines, do not show any prominent photocentre shift in the emission maps (Fig. 3). However, photocentre shifts are clearly detected in the fits (Fig. 8). For Pa β and Bry, our calculation shows that this emission displacement along the X -direction is not detected, while it is large in the Y -direction (along the jet axis), the same for the [Fe II] lines. The position of the continuum photocentre is quite flat for the Pa β and the H₂ line at 2.406 μm , but for Bry and H₂ at 2.122 μm there was a noticeable slope, which was removed by linear fitting during the calculation. In general, the photocentre on the Bry line demonstrates the same behaviour as the [Fe II] lines: the photocentre has a small shift ($\sim 0''.02$) for the blueshifted lobe (upper jet lobe in Fig. 3), but a much larger shift in the longer red jet lobe. Our fitting shows a displacement of $0''.07$ (~ 13 au) for the Bry line in the red lobe. At the same time, after the line-to-continuum correction, the Pa β line shows almost the same shift in both jet directions ($0''.15$ for the blueshifted lobe and $0''.13$ for the redshifted lobe). These results indicate that the gaseous structures traced by the atomic lines are probably affected in the regions where the jet forms and that the atomic gas is entrained by the inner jet.

We also fit the circular cores of the spatial profiles for the bright H₂ lines at 2.122 and 2.406 μm centred on the star and calculated the photocentre displacement with respect to the continuum, also shown in Fig. 8. Both lines exhibit a slight shift along the jet axis (Y -direction). Their calculated centroid shows a similar shift (1.5 and 1.7 pix), which corresponds to an average angular shift of $\sim 0''.08$ (~ 15 au). At the same time,

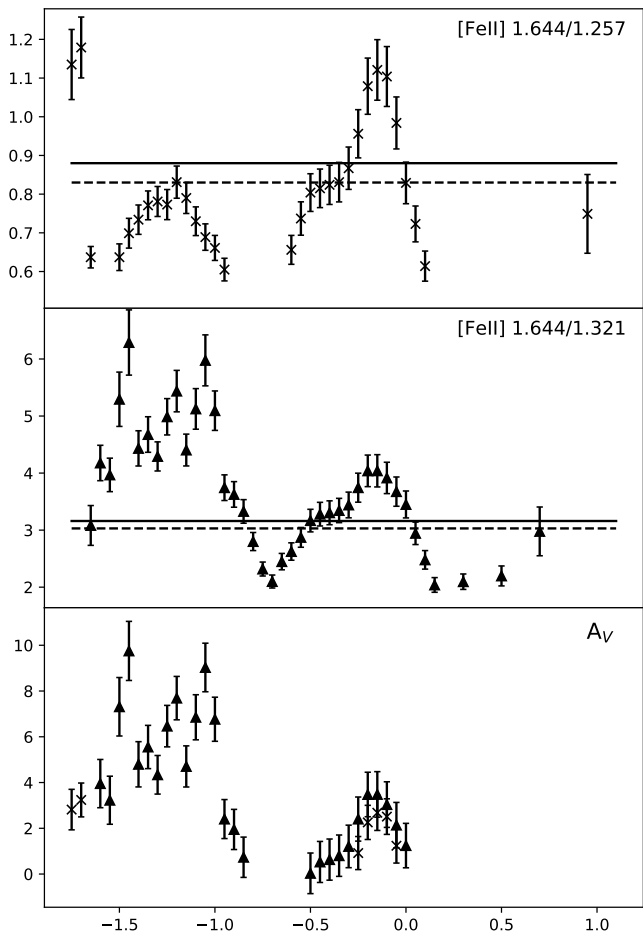


Fig. 7. Visual extinction A_V along the Th 28 jet calculated from [Fe II] 1.644/1.257 and 1.644/1.321. The theoretical intrinsic ratio for $A_V = 0$ from Smith & Hartigan (2006) is shown by the solid line, whereas the empirical intrinsic ratio determined by Giannini et al. (2015) is shown as the dashed line. The error bars are calculated from the RMS errors plus an uncertainty of 30% for the determination of the Einstein A coefficient and an uncertainty of 10% linked with the flux calibration. The extinction A_V (lower panel) is calculated for all positions, showing the ratio value above the theoretical intrinsic [Fe II] ratio.

both lines also reveal a small displacement in the disc plane (X -direction). We took into account the line-to-continuum ratio only for the X -shifts of the H_2 2.406 μm line, because the X -shift of H_2 2.122 μm line is too small for this correction. Both lines show a slight redshifted Y -displacement, whereas their X -offset is blueshifted and weaker than in the Y -direction. The width of the H_2 displacement is smaller than that of the [Fe II] lines and the atomic hydrogen lines. After line-to-continuum correction, the computed photocentre shift in the Y -direction of the faint H_2 2.413 μm line (Fig. 8) has an amplitude similar to the brighter H_2 lines ($\sim 0''.06$ or ~ 11 au). However, unlike the brighter H_2 lines, the H_2 2.413 μm line does not exhibit any displacement in the X -direction.

To summarise, all bright emission lines reveal that the maximum gaseous emission is shifted along the redshifted jet, with the largest shift seen in the [Fe II] lines, tracing the jet beams. Both the atomic and molecular hydrogen lines also have detectable shifts in the same direction as the red lobe of the jet. The photocentre displacements of the $\text{Pa}\beta$ and $\text{Br}\gamma$ emission regions, which are usually small and unresolved, imply that

the HI emission traces the material entrained by the jet or is due to atomic gas from the jet themselves. These results also reveal a prominent asymmetric spectroastrometric signal in the redshifted jet, compared to the (slower) blueshifted jet.

3.5. Morphology of the H_2 emission

Unlike the [Fe II] emission, which traces the collimated jet lobes, the spatially resolved emission in the H_2 lines shows a flattened arc-like structure, orthogonal to the direction of the jet axis. In the brightest lines this H_2 emission covers the entire FoV in the north–south direction (see Fig. 3 and Fig. 5). However, this region may be even larger because the H_2 emission at 2.12 μm , for instance, is still bright (Fig. 3) at the edges of the SINFONI FoV ($3'' \times 3''$, ~ 540 au \times 540 au at the adopted distance of Th 28). Therefore, the H_2 emission has a size of at least 540 au. If we exclude the region of faint emission at the periphery, the emission around the central star has a bright inner core, with a transverse width of about $1''.5$ (~ 135 au).

Our fitting of this core in several bright H_2 lines shows that the extension of this core in the X -direction (disc plane) is slightly larger than in the Y -direction (jet axis) for all the fitted lines. For instance, at 2.122 μm H_2 has $FWHM_X = 0''.383$, but $FWHM_Y$ is $0''.372$. The difference between X and Y is small ($\sim 3\%$), but visible in almost all H_2 lines; even after excluding the faint emission periphery, the central H_2 core has a flattened shape aligned with the plane of faint peripheral emission and therefore with the circumstellar disc. The FWHM of the continuum around the H_2 2.122 μm line is the same in both directions (i.e. $FWHM_X = FWHM_Y = 0''.325$), and it is smaller than that of the line centre. We calculated the total flux against the wavelength for three bright molecular lines in the K band, H_2 1.958, 2.122, and 2.413 μm , and fit the 1D emission line profiles to calculate their FWHMs. The fitted $FWHM_{in}$ of H_2 2.122 is ~ 50 km s^{-1} (Fig. 9), which is narrower than $\text{Br}\gamma$ and $\text{Pa}\beta$ (internal $FWHM_{RV}(H_2$ 1.958) = 89 km s^{-1} and $FWHM_{RV}(H_2$ 2.407) = 43 km s^{-1}). The morphology of the H_2 emission (Fig. 3) differs from that of [Fe II], which clearly traces the outflow structure. The fitted peak RV for H_2 2.122 μm is centred at 5 km s^{-1} , which differs from the result of Coffey et al. (2010) who found a blueshifted velocity of about -10 km s^{-1} for the H_2 emission in the direction of both the receding and approaching jet lobes. We try to explain the H_2 RV shift analysing the H_2 PV diagram along the jet axis (see Fig. 10). We also note that Coffey et al. (2010) did not resolve the H_2 emitting region from the measurement along the jet, while for the slit position perpendicular to the jet, the H_2 emission is clearly resolved (see Figs. 3 and 7 in their article). This agrees well with our results from the SINFONI data.

Using our SINFONI observations, we calculated the PV maps of the H_2 2.122 μm line both along (Fig. 10) and perpendicular to (Fig. 11) the direction of the jet to explore the kinematics of molecular hydrogen emission. Although our 2D images show that H_2 emission is concentrated mainly in the plane orthogonal to the jet axis, the PV map along the jet axis shows hydrogen emission up to $\pm 1''.5$ away from the jet source. This scale is about twice the radius of the bright compact core. The H_2 2.122 μm emission distribution along the jet axis is, in general, similar to that seen on the more extended PV map (Fig. 2 from Coffey et al. 2010), which traces H_2 emission up to $\sim 2''$ in both jet lobes. The H_2 emission does not show a brightness asymmetry between the blue and red lobes, as seen in the forbidden lines, which also agrees well with the result of Coffey et al. (2010). The

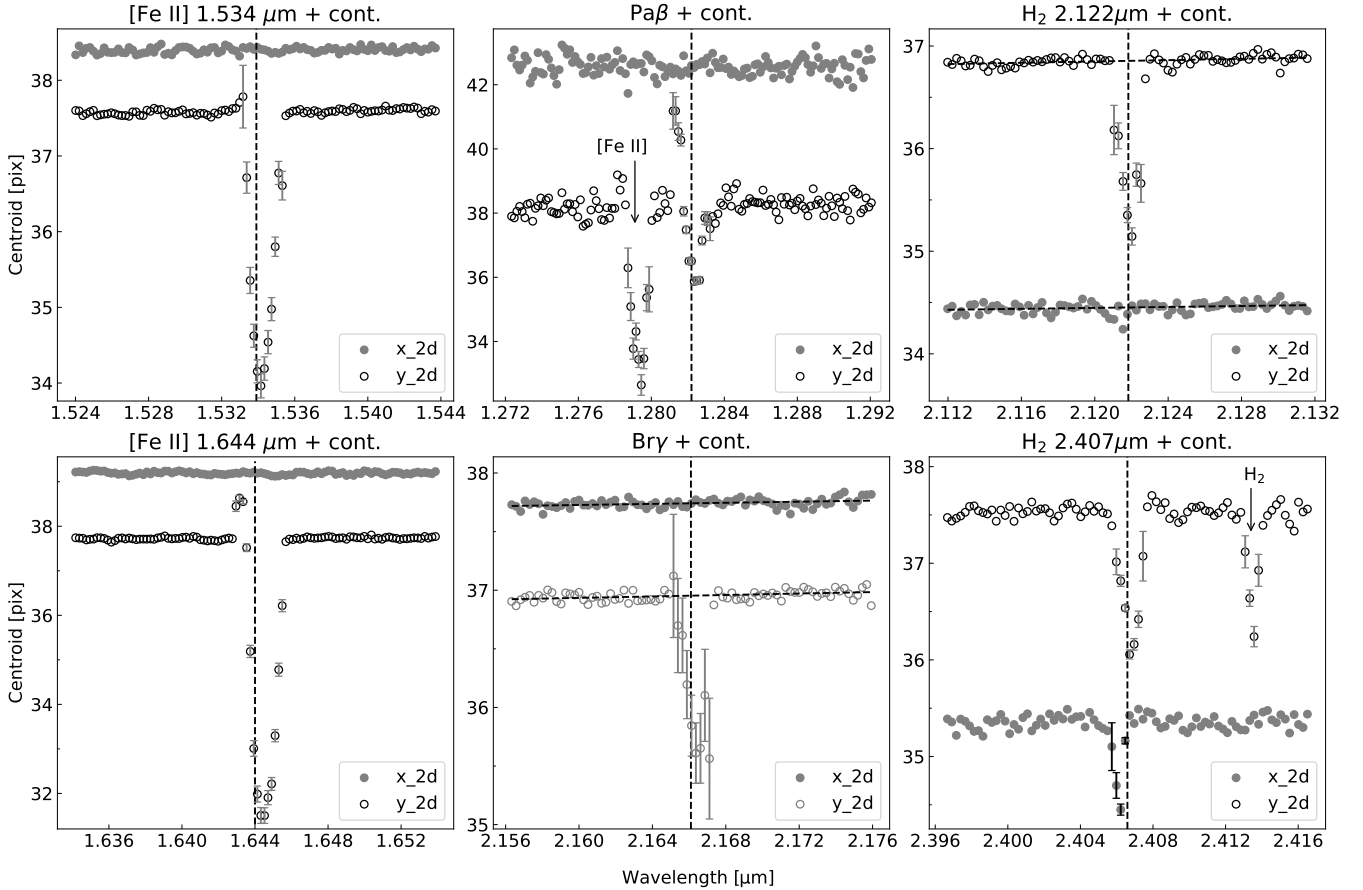


Fig. 8. Photocentre shift for [Fe II] 1.534, 1.644 μm , Pa β , Bry, and H₂ 2.122, 2.406 μm along the XY-directions. The Y-direction is aligned with the jet axis, whereas the X-direction is orthogonal. The wavelength of spectral lines in the vacuum is indicated by vertical lines. On some plots, the values of centre coordinates are shifted as a whole in order to place both distributions on the same plot. The instrumental bias around Bry, calculated from the continuum, was fit with a linear function (shown as dashed lines) and removed from further analysis. The shifts in the line cores were corrected for the line-to-continuum ratio, and the errors derived for the line centre displacement are shown. All the emission lines display a significant photocentre shift along the Y-direction (the direction of the jet), whereas the H₂ lines also show a small shift in the orthogonal direction (X).

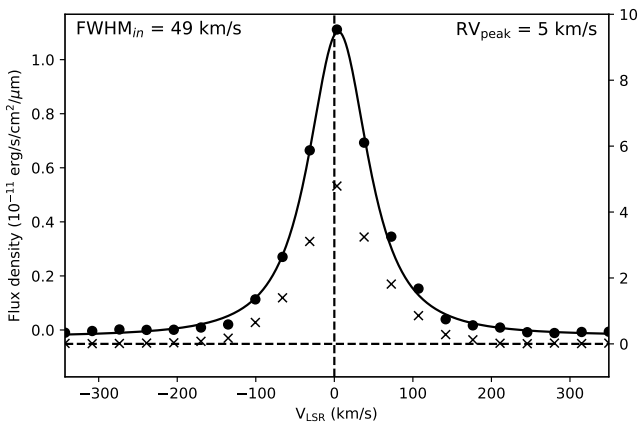


Fig. 9. Fit of the line profile of the H₂ 2.122 μm line ($FWHM_{in} = 49 \pm 11 \text{ km s}^{-1}$) integrated over the central region using a Moffat function (solid black line). The peak of the emission profile is redshifted by $\sim 5 \pm 2.7 \text{ km s}^{-1}$ with respect to the system velocity of $\sim 3 \text{ km s}^{-1}$ (dashed vertical line). The S/N computed for each position is indicated with a cross. The S/N scale is shown on the right y-axis, and the dashed horizontal line indicates the zero level.

distribution of RV_{peak} and $FWHM_{in}$ along the jet derived from fitting the PV diagram are shown as a function of distance

from the source. Fitting the H₂ emission profiles has smaller errors for the distance from the jet source $< 0''.7$, but the fitting errors increase at larger distance from the source due to the poorer S/N of the line (Fig. 10). In general, the PV diagram does not show a significant difference between the H₂ gas velocity along the jet at distances $> 0''.5$ compared to the internal regions $< 0''.5$. The average values of the parameters computed at all positions with reliable fitting are $RV_{\text{peak}} = 4.6 \pm 1.9 \text{ km s}^{-1}$ and $FWHM_{in} = 42.4 \pm 4.7 \text{ km s}^{-1}$ and both values are marked in Fig. 10 by vertical lines. The distribution of RV_{peak} values along the jet is very close to the mean value, and there is no significant difference between the red and blue lobes. Therefore, the $RV_{\text{peak}} \sim 5 \text{ km s}^{-1}$ visible in other RV diagrams (Figs. 9 and 11) probably represents a systemic shift resulting from errors in the wavelength calibration. However, we can draw some conclusions. In particular, the rest RV of the H₂ emission in the jet lobes is very small, and therefore the total H₂ velocity in the jet should also be small. There are a few points at distant positions where the RV sign agrees with the sense of the inclination of the jet lobes (i.e. H₂ 2.122 μm has the negative RV for the approaching lobe and the positive values for the receding one). However, the measurement errors for these positions are also high.

The PV diagram of the H₂ line along the direction perpendicular to the jet axis is also similar to that of Coffey et al. (2010, see their Fig. 7). The horizontal dashed line shows the

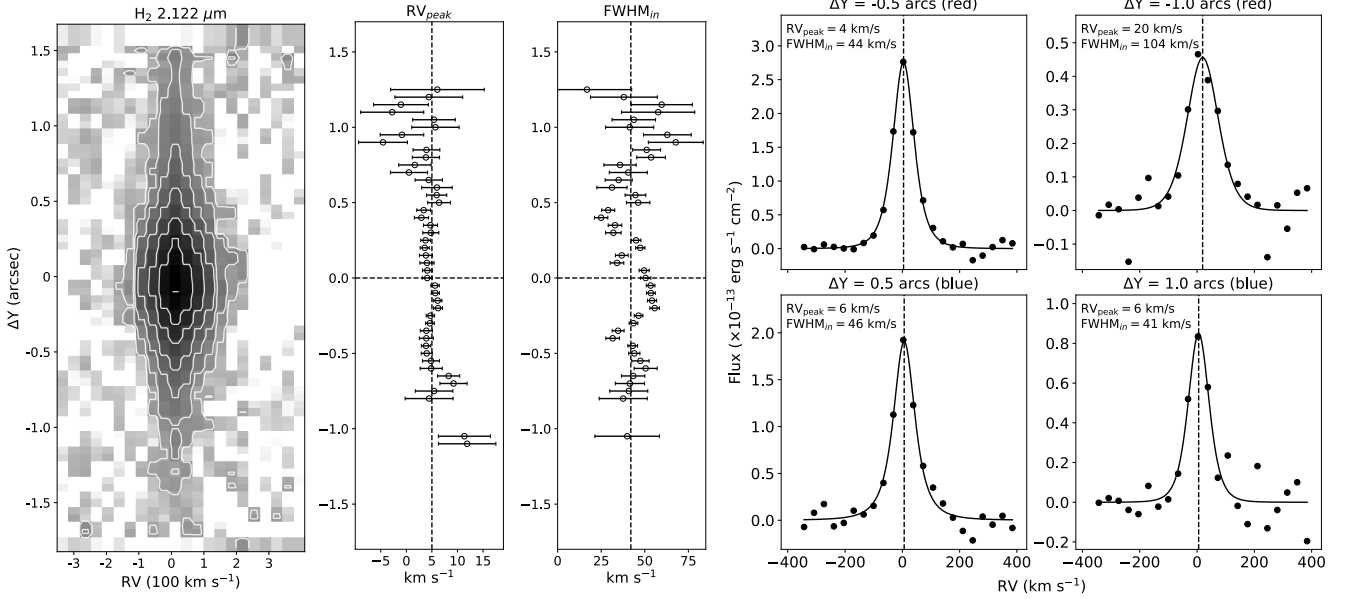


Fig. 10. Distribution of the H_2 2.122 μm emission along the jet. Left image: PV diagram of the H_2 2.122 μm line along the jet axis of Th 28, obtained by integrating the fluxes in the 22 spectral frames over the direction perpendicular to the jet. Logarithmic contours are drawn from $2 \times 10^{-14} \text{ erg s}^{-1} \text{ cm}^{-2} \text{ arcsec}^{-2} \text{ \AA}^{-1}$, with an incremental logarithmic step of 0.3 dex. Two central panels show the derived RV_{peak} and $FWHM_{\text{in}}$ as a function of distance from the source. A vertical line at 5 km s^{-1} in the RV panel marks possible systemic RV shift for the line; an average value of $FWHM_{\text{in}}$ is 43 km s^{-1} (vertical line). Right four panels: Spectral profiles across the jet at selected positions within an $\pm 1''$ area in the blue and red lobes (black points). The data were fit using a Moffat function (solid line); the derived peak RV and intrinsic FWHM are shown at the top of each panel.

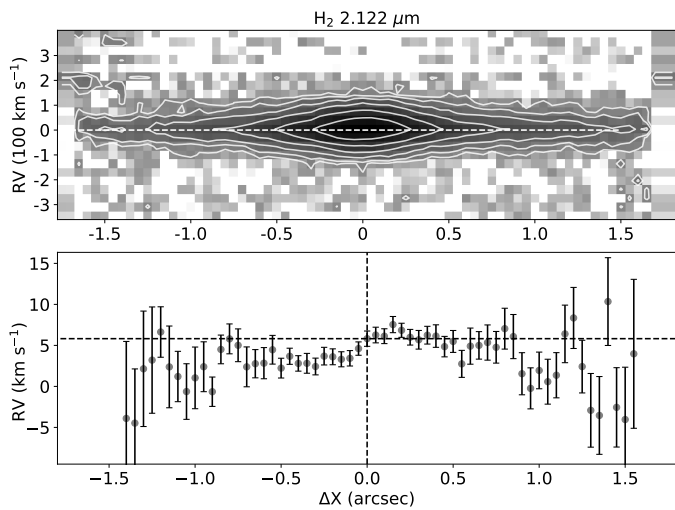


Fig. 11. Distribution of the H_2 2.122 μm emission in the disc plane. Upper panel: PV diagram of the H_2 2.122 μm line perpendicular to the direction of the jet axis and in the disc plane. Lower panel: Peak radial velocities with error bars computed from fitting across the PV diagram at every position with $0.05''$ steps. The region from $-0.75''$ to $0.75''$ around position at $0''$ corresponds to the bright core of H_2 emission around the jet source.

RV of the H_2 gas derived at the stellar position (5.4 km s^{-1}). The size of the region from $-0.75''$ to $0.75''$ corresponds to the bright core of H_2 emission around the jet source. The RV uncertainties are quite small for this central region and then increase towards the periphery of the H_2 emission region. If we consider the bright emission region, we note that the left part (from $-0.75''$ to $0''$) shows a systematically lower RV value than the opposite one (from $0''$ to $0.75''$) which can be an indication of

gas rotation in a circumstellar disc. Both the direction and the magnitude of the velocities are similar to that derived from CO emissions that was interpreted as the rotation of the circumstellar disc (Louvet et al. 2016). However, the current spectroscopic resolution does not allow us to draw any conclusions about the Keplerian rotation in the disc. Taking the error bars into account, the PV map does not show a large departure of RVs along the disc plane direction from the velocity at $0''$. The average $FWHM_{\text{in}} = 47.3 \pm 4.0 \text{ km s}^{-1}$ within $-0.75''$ to $0.75''$ along the disc plane is slightly higher than the value measured along the jet. The RVs observed in the faint peripheral H_2 emission (at radial distances $>0.75''$) seem to deviate from that of the central region and are consistent with zero, but the measurement errors are higher for those positions as well.

Analysis of the morphology of H_2 emission, as well as gas parameters, shows that many YSO outflows and jets are associated with molecular hydrogen emission generated by gas shock waves (Beck et al. 2008, and references therein). However, some YSOs also show the presence of quiescent molecular hydrogen emission, probably of fluorescent origin (Beck et al. 2008). Therefore, the origin of the H_2 emission requires special consideration, which we discuss in Sect. 4.

3.6. Physical parameters of the H_2 emission region

The H_2 transitions that arise from the same upper state of the H_2 molecule can be used for the determination of A_V . For example, bright H_2 lines such as the $\nu = 1 - 0 \text{ S}(1)$ at $2.122 \mu\text{m}$ and $\nu = 1 - 0 \text{ Q}(3)$ at $2.424 \mu\text{m}$ are both detected in the spectrum of Th 28. The intrinsic $\text{Q}(3)/\text{S}(1)$ line ratio of 0.7 is not affected by the physical conditions of the gas-emitting environment. At the same time, A_V calculations based on the H_2 line ratios have a very strong dependence on the values of the ratio (e.g. Davis et al. 2011). Taking the integral fluxes of these

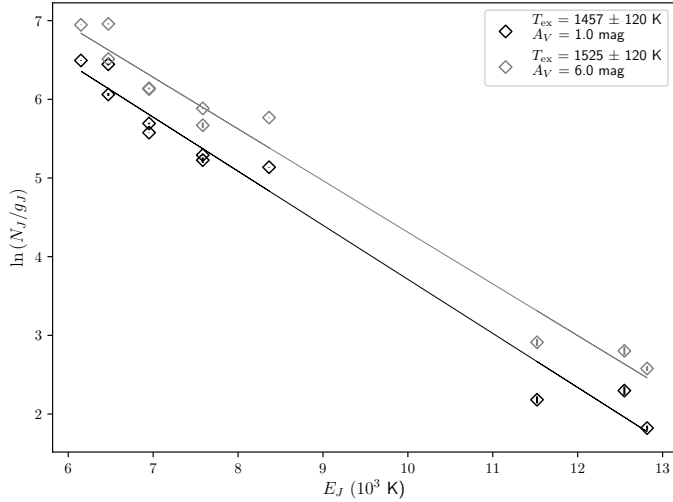


Fig. 12. Rotation diagram for H₂ lines in the central (0′′.25 × 0′′.25) region of Th 28. The solid lines show the best fit to the logarithm of column density vs upper energy level. Two colours represent the impact of different values of A_V on the excitation temperature. $A_V = 1.0$ mag is taken from [France et al. \(2012\)](#); $A_V = 6.0$ mag is derived from the I_{S1}/I_{Q3} relation.

lines within a central emission core of 1′′ × 1′′ in size and the relation $A_V = -114 \times \log(0.704 \times [I_{S1}/I_{Q3}])$ from [Davis et al. \(2011\)](#), we find a mean extinction of $A_V = 6 \pm 0.3$ mag for this region. This result differs from the value of $A_V = 1.1$ mag derived from the pre-main-sequence stellar evolutionary tracks of [France et al. \(2012\)](#). The last result is based on photometry, probably obtained with a much larger aperture and therefore less affected by absorption in the circumstellar disc.

The excitation temperature of H₂ can be estimated using the rotational diagram method. For a Boltzmann distribution between energy levels $N_J/g_J \sim e^{E_J/kT}$, where N_J , g_J , E_J , and T are column density, statistical weight of the transition, upper-level energy, and excitation temperature, respectively. This implies that a local thermodynamic equilibrium (LTE) has been established in our system. The column density may also be expressed through flux as $N_J = 2F_J\lambda_J/A_Jhc$, where F_J , λ_J , and A_J are the dereddened flux, line wavelength, and the Einstein coefficient of each transition, respectively. For dereddening, we used the extinction law of [Cardelli et al. \(1989\)](#) with $R_V = 3.1$ (see below for an additional discussion on the values of A_V). In Fig. 12, we show the dependence of the natural logarithm of the H₂ column density of each level on the energy of the upper level for the central region, integrated in 0′′.25 × 0′′.25. The uncertainties were calculated using the bootstrap method by randomly varying the flux values with a normal distribution over their measured uncertainties and finding the dispersion of the resulting temperatures after optimisation. The temperature map obtained is shown in Fig. 13. Values range approximately from 1000 K to 2500 K.

This Boltzmann diagram method could also be used as another way to determine interstellar extinction, simultaneously with the evaluation of excitation temperature. In our case, the extinction values obtained were sporadic from pixel to pixel; therefore, we used this method only to determine the excitation temperatures. As seen in Fig. 12, extinction values affect the temperature only within the error margin, which is why the temperature can be determined under the assumption that the excitation is constant.

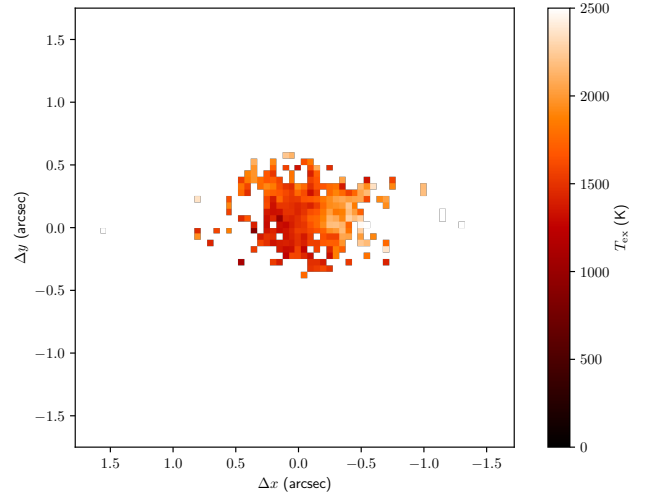


Fig. 13. H₂ excitation temperature map. The values from 0 to 2500 K in linear scale are colour-coded from dark to light (see colour scale at right). All data points selected have at least nine molecular hydrogen lines with flux $>2\sigma$.

4. Discussion

The high-resolution 2D SINFONI spectra allowed us to study the morphology of gas emission formed in different gas structures around Th 28. Three groups of emission lines were detected in NIR spectroscopy: forbidden iron lines, atomic hydrogen lines, and molecular hydrogen lines. Some of our results are similar to those of the detailed study done by [Coffey et al. \(2010\)](#) based on the analysis of a similar set of emission lines and 1D slit spectra. In that study line fluxes and radial velocities are probably more sensitive because of the long-slit observations, which have higher spectral resolution. However, the 2D SINFONI maps give us a closer look at the spatial distribution of the emission at high angular resolution.

4.1. Origin of [Fe II] emission

The [Fe II] lines are emitted by a well-defined outflow, which is extended and coincident with the jet, as traced by [S II] ([Wang & Henning 2009](#)). The brightness distribution of [Fe II] along the bipolar jet obtained from the 2D maps confirms the jet asymmetry visible in the [S II] map, and coincides in general with the results of [Coffey et al. \(2010\)](#). In the vicinity of the central source, the [Fe II] emission is distributed approximately uniformly in the jet column, but forms emission knots on both sides of the source at a distance of $\sim 1''$, which were not detected by [Coffey et al. \(2010\)](#). More distant emission knots were also found by [Wang & Henning \(2009\)](#), but are outside our observed FoV.

The emission in the iron lines allows us to trace the change in the geometry of the jet. We integrated the flux of the bright [Fe II] 1.644 μm line over all frames from -220 km s^{-1} to $+240 \text{ km s}^{-1}$. Figure 14 shows the width of the jet measured using the [Fe II] 1.644 μm line as a function of the distance from the central source. The observed FWHM is measured with a Gaussian fit perpendicular to the jet axis. The intrinsic jet width is calculated as the observed FWHM corrected for the $FWHM_{\text{PSF}} = 0'':23$ derived around the [Fe II] line (i.e. $FWHM_{\text{jet}}^2 = FWHM_{[\text{Fe II}]}^2 - FWHM_{\text{PSF}}^2$). Data were masked at a level of 3σ . To estimate the size of the jet cone at its base, we fit each of the lobes with a power function $f(x) \propto (x - C)^n$, which are shown in the plot.

These approximations reveal a change in the geometry of the red jet lobe at about $0''.5$ from the central source. A similar change is seen in the blue lobe of the jet, but there is already a significant deformation of the jet shape at $0''.6$, probably due to the disc–jet interaction, and therefore the fit is not applicable. At around $0''.9$, however, the collimation of the red jet lobe seems to change again and the diameter of the jet stops growing and becomes more stable. A similar behaviour is detected in some other YSO jets; the width of the jets first increases with increasing distance from the jet source, but at certain distances it stops growing and its collimation stabilises (e.g. the width of the RW Aur jet stabilises at $\sim 1''.5$ from its source; [Woitas et al. 2002](#)). Therefore, at larger distances the Th 28 jet is found to be more collimated, as measured by [Murphy et al. \(2021\)](#).

Using the approximation function for the jet width, an upper limit to the maximum possible size for the jet formation region is now available by calculating the diameter of this function at the level of the accretion disc. The maximum radius of the jet at the disc position is estimated to be $\sim 0''.015$, corresponding to a jet launching radius of ~ 3 au. This estimate represents an upper limit of this value due to the high uncertainty of the extrapolation and is higher than that derived by [Ferreira et al. \(2006\)](#). At the same time, this is less than the maximum launch radius ($r_{\max} \simeq 5$ au) adopted in the magnetohydrodynamic jet models of [Ray et al. \(2007\)](#).

We used a simple linear fit to estimate the full opening angle for both outflow lobes in Th 28. For the full range of iron emission velocities, we found that within the first $0''.6$ the opening angle is $\sim 28^\circ \pm 2^\circ$ for both lobes, while the red lobe within $0''.9$ shows a mean opening angle value of $\sim 35^\circ \pm 3^\circ$. The derived opening angle also depends on the velocity range. For example, [Agra-Amboage et al. \(2011\)](#) found that the medium velocity gas ($< 150 \text{ km s}^{-1}$) in the DG Tau jet is collimated inside a cone with a full opening angle of 28° , similar to that of Th 28, whereas the high-velocity gas ($> 150 \text{ km s}^{-1}$) in the jet is more collimated and has a full opening angle of 8° . We computed the opening angles in the Th 28 jet for two velocity ranges, for emission with a velocity $> 100 \text{ km s}^{-1}$ and with a velocity $< 100 \text{ km s}^{-1}$. We found that at high velocities, the gas in the blue lobe appears to be more collimated with a full opening angle of $20^\circ \pm 3^\circ$, which increases to $\sim 30^\circ \pm 4^\circ$ at low velocities. At the same time, in the red lobe the gas emission has a similar collimation ($\sim 27^\circ \pm 4^\circ$) for both velocity ranges. Therefore, the Th 28 jet appears to be less collimated than some other YSO jets, with an opening angle of $5\text{--}10^\circ$ near the jet source ([Bacciotti et al. 1999](#); [Woitas et al. 2002](#); [Dougados et al. 2004](#)). At the same time, the DG Tau jet ([Woitas et al. 2002](#)) also shows a steep increase in jet width, which is similar to the Th 28 red lobe case.

An interesting feature of the [Fe II] RV distribution is the presence of opposite motion for both jet lobes: channel maps exhibit a blueshifted emission gas for the redshifted lobe, and vice versa. Taking into account the estimated full opening angle (see the discussion of Fig. 14), a natural explanation for this seemingly contradictory result is that the jet cone has a position on its axis close to the sky plane. In this case, we see various velocity components of diverging streams and/or transverse motion resulting from rotation. With the adopted inclination of the jet axis and a half-opening angle of 14° obtained within the first $0''.6$, the outflow cone would remain completely behind the plane of the sky. Therefore, this opening angle would not be large enough to explain the blueshifted emission in the redshifted flow (Sect. 3.2). However, with a half-opening angle of $\sim 18^\circ$ the outflow cone would reach the front side of the plane of the sky

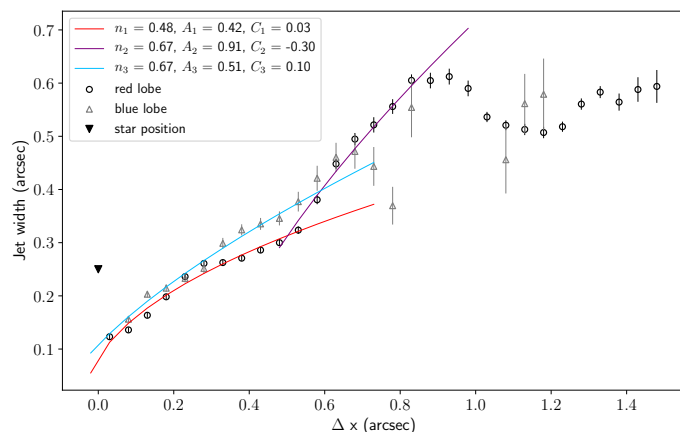


Fig. 14. Jet width vs distance from the central source at $1.644 \mu\text{m}$. The intrinsic jet width is computed with $FWHM_{\text{PSF}} = 0''.23$ derived from the continuum images around the line. Data from the red and blue lobe of the jet are indicated by grey triangles and black circles, respectively. The solid lines are approximation functions $f(x) \propto (x - C)^n$, where C is a free parameter and n is a degree, which demonstrates the change in geometry of the jet for the red lobe.

and create a quite prominent negative velocity flow component visible between $0''.5$ and $1''.5$ in the red jet lobe.

Various magnetohydrodynamic jet-launching models (e.g. [Ferreira 1997](#); [Ferreira et al. 2006](#); [Pudritz et al. 2007](#)) predict the presence of gas flows with different velocities close to the source position, including low-velocity uncollimated outer streams. For example, [Garcia Lopez et al. \(2008\)](#) found that the atomic and molecular gas (seen in [Fe II] and H_2 lines) at the base of HH 34 jet show two components at high velocities (HVC) and low velocities (LVC), which trace the jet and disc wind, respectively. Due to the high inclination of the jet in Th 28, the measured RVs of the [Fe II] jets are also relatively small, and therefore these lobes are only weakly spectrally resolved in the channel maps. We did not find any indication of low or high components in the redshifted jet. [Coffey et al. \(2010\)](#) also did not report any distinction between the high- and low-velocity components. However, the fact that RV increases along the blue lobe may imply that both LVC and HVC could be present at the base of the jet. The emission could be dominated by the LVC at the jet base and the HVC further away. This is also supported by the fact that in the blue jet the [Fe II] line widths are substantially larger at the base of the flow, suggesting the presence of an additional component of the HVC. This is also supported by the presence of [O III] $\lambda 5007 \text{ \AA}$ in the blue lobe, as reported by [Comerón & Fernández \(2010\)](#), who associated this emission with stellar winds.

In general, the [Fe II] emission at $1.644 \mu\text{m}$ covers redshifted velocities up to $\sim 240 \text{ km s}^{-1}$, which is similar to that of the opposite lobe ($RV_{\max} \sim 220 \text{ km sec}^{-1}$). From the fit to the line profiles, we adopted $RV_{\text{peak}} = 41 \pm 0.8 \text{ km s}^{-1}$ and $-105 \pm 7.5 \text{ km s}^{-1}$ at $+1''$ for the red- and blueshifted lobes, respectively (see Fig. 6). This difference is consistent with previous studies, which reported that RVs of HH objects in the blueshifted jet are greater by an average factor of 1.5–2 compared to those in the redshifted jet ([Comerón & Fernández 2010](#); [Murphy et al. 2021](#)). If we adopt the different inclination angles for the opposite jet lobes measured by [Murphy et al. \(2021\)](#) ($i_{\text{red}} = 83^\circ.5$ and $i_{\text{blue}} = 77^\circ$), the deprojected gas velocity for the emission will be similar for the two beams, $\sim 360 \text{ km s}^{-1}$ for the redshifted lobe and $\sim 470 \text{ km s}^{-1}$ for the blueshifted lobe.

The deprojected velocities calculated from the velocities measured by [Murphy et al. \(2021\)](#) are $\sim 270 \text{ km s}^{-1}$ for the redshifted lobe and $\sim 360 \text{ km s}^{-1}$ for the blueshifted lobe (i.e. $\sim 100 \text{ km s}^{-1}$ less than our results). For our RVs this difference is $\sim 10 \text{ km s}^{-1}$. We suggest that this RV discrepancy can be partly explained by a systemic shift between these wavelength calibrations. In any case, this deprojected velocity implies that the Th 28 jet is quite fast among the YSO jets because the YSO jets usually show gas velocities between 50 and 400 km s^{-1} ([Ferreira et al. 2006](#)).

One of the interesting features of the data is a prominent brightness asymmetry in the opposite jet lobes, visible in [Fe II]. One of the possible origins suggested for such an observed jet brightness asymmetry could be an occultation by a circumstellar disc (e.g. [White et al. 2014](#)), which partially blocks the radiation from one of the jet lobes. However, the observed jet structure in Th 28 does not support this scenario. The circumstellar extinction in the direction to Th 28 does not seem to be high. From the analysis of the H_2 emission, we estimate the $A_V \approx 6$ mag, while [France et al. \(2012\)](#) found $A_V = 1.1$ mag based on photometry. This agrees with the fact that we do not see any evidence of a dark lane in Th28, as seen in the DG Tau system (Fig. 1 in [Agra-Amboage et al. 2014](#)). Moreover, the redshifted jet is brighter than the blueshifted jet, whereas in the case of disc occultation, we would see the opposite effect.

Another possibility to explain the observed jet emission structure is the orientation of its natal cloud, where the blueshifted jet lobe penetrates into the dense part of the cloud, while the redshifted jet propagates into a lower-density environment. To verify this, we measured the fluxes for the $\nu = 1-0 \text{ Q}(3)$ and $\nu = 1-0 \text{ Q}(1)$ H_2 lines, and calculated their ratios to the $\nu = 1-0 \text{ S}(1)$ line. The first two H_2 lines can also be detected along the blue lobes up to $1''.5$ as $\text{H}_2 2.122 \mu\text{m}$. At the same time, the bright [Fe II] $1.644 \mu\text{m}$ line in the blue lobe becomes fainter after $0''.5$ and disappears completely after $1''$. If the [Fe II] line weakening is caused by extinction, I_{Q3}/I_{S1} should also change accordingly. However, the distribution of the H_2 ratio is flat and does not show any gradient. The mean value of the H_2 ratio for both lobes is 0.79 ± 0.21 , which corresponds to $A_V = 6$ mag. The I_{Q1}/I_{S1} distribution along the jet axis is also flat. Therefore, we suggest that the observed brightness asymmetry of the [Fe II] line has an intrinsic origin, rather than due to changes in extinction along the blue lobe (i.e. the asymmetry is caused by the engine, rather than the medium).

4.2. Origin of Pa β and Br γ emission

The origin of atomic hydrogen emission around the YSOs is still being debated. The theory predicts that the Pa β and Br γ lines should form close to the star due to accretion. In fact, the luminosity of hydrogen lines has been found to correlate strongly with the accretion luminosity in classical T Tauri stars ([Muzerolle et al. 1998](#)) and in young brown dwarfs ([Natta et al. 2004](#)). [Garcia Lopez et al. \(2008\)](#) reported wide Br γ emission in the spectrum of HH 34, which, nevertheless, does not show spatial extension along the jet.

However, there is some evidence that this permitted emission can also trace young stellar jet activity ([Whelan et al. 2004](#); [Beck et al. 2010](#); [Caratti o Garatti et al. 2016](#)). For instance, [Beck et al. \(2010\)](#) spatially resolved extended Br γ emission in several outflows from young stars, and associated the emission with known HH objects. In the case of the Th 28 jet, [Coffey et al. \(2010\)](#) concluded from the high-resolution 1D spectroscopy analysis that a component of the Pa β and Br γ emission comes from the outflow. In the present work, Pa β emission

is clearly resolved in the redshifted jet lobe. The presence of atomic hydrogen emission in the jet and HH objects is important because these permitted transitions originate in high-density gas regions where forbidden lines are quenched ([Coffey et al. 2010](#)).

The 2D SINFONI flux maps demonstrate that the H I emission in Th 28 probably consists of two components. In addition to the bright Pa β and Br γ emission regions with roundish shapes, there is also a faint component stretching along the jet axis. As in the case of other YSOs, the emitting region of atomic hydrogen is very compact. Pa β ($FWHM = 0''.72 \pm 0''.04$) and Br γ ($FWHM = 0''.33 \pm 0''.03$) are barely resolved, with angular sizes similar to those of continuum emission ($FWHM_J = 0''.68$ and $FWHM_K = 0''.32$). At the same time, the RVs of the Pa β and Br γ emission, integrated over the compact bright atomic hydrogen core, are shifted toward the red, although their peak RVs are clearly lower than those of [Fe II]. The measured redshifts of RV in Pa β (34 km s^{-1}) and Br γ (18 km s^{-1}) are similar to those obtained by [Coffey et al. \(2010\)](#) for the red lobe, and can trace the gas in the descending jet lobe, which is brighter than the blue lobe. Additionally, the redshifted emission can be partly caused by infalling material in the accretion columns. This infalling gas detected in emission lines is assumed for the magnetospheric accretion model, as suggested by observations and modelling of other YSOs ([Muzerolle et al. 1998](#); [Tambovtseva et al. 2016](#)).

On the other hand, there is a fainter emission component that is spatially resolved and extends along the outflow direction (Fig. 3). The signs of faint emission are visible in both directions outside the bright H I emission core. Therefore, both formation scenarios (accretion and jet activity) of atomic hydrogen emission likely contribute to the case of Th 28. However, the spectral resolution of our observations is not high enough to discriminate between these two scenarios. We obtain only the general distribution of RV, and do not resolve any velocity components. The atomic lines have wide emission profiles ($\gtrsim 250 \text{ km s}^{-1}$), which supports the presence of a high-velocity component.

4.3. Investigating the origin of H_2 emission

Many collimated young stellar outflows and jets and associated HH objects exhibit molecular hydrogen emission. There are several explanations for the presence of extended H_2 emission in the NIR around YSO with jets. The primary excitation mechanisms are (1) H_2 emission excited by shock waves, (2) thermal excitation by UV and X-ray radiation ([Gustafsson et al. 2008](#)), (3) irradiation of fluorescent quiescent H_2 due to the IR cascade of non-thermal pumping by $\text{L}\alpha$ ([Beck & Bary 2019](#)), and (4) excitation via ambipolar diffusion ([Frank et al. 1999](#)). There are various scenarios for the formation of spatially extended H_2 emission in different gas structures of T Tauri stars. For example, shocks seem to be more responsible for the excitation of H_2 emission that originates in the jet lobes ([Beck & Bary 2019](#)). Several scenarios are assumed for the origin of the wide-angle H_2 emission, which can originate in a circumstellar disc of a YSO (see Fig. 10 in [Agra-Amboage et al. 2014](#)).

The first detections of the $\nu = 1-0 \text{ S}(1)$ ro-vibrational transition of H_2 at $2.12 \mu\text{m}$ in the spectrum of HH objects were identified as shock-excited emission ([Beckwith et al. 1978](#); [Elias 1980](#); [Burton et al. 1989](#); [Wilking et al. 1990](#)). [Beck et al. \(2008\)](#) listed some highly collimated T Tauri jets revealing shock-excited H_2 emission in their jet lobes. [Caratti o Garatti et al. \(2015\)](#) studied 18 massive jets driven by intermediate-mass and high-mass YSOs and found that all the flows analysed show H_2 emission lines that originate from shocks at high temperatures and densities. A recent high-resolution study of massive YSO

G192.16-3.82 also detected H₂ emission in a chain of tightly collimated knots, implying its shock origin (Boley et al. 2019).

However, Bary et al. (1999) detected molecular hydrogen gas around CTTS TW Hya, which appears to be concentrated in its circumstellar disc. They found that this H₂ emission is fluorescent in origin, induced by X-ray radiation. Therefore, this fluorescence from quiescent molecular hydrogen gas may be expected in other X-ray bright T Tauri stars. Furthermore, Bary et al. (2003b,a) discovered this quiescent H₂ emission towards several CTTs, and concluded that it is most likely located in a disc orbiting the young star. Takami et al. (2004) detected NIR H₂ emission around DG Tau, which is of an age (~1–2 Myr, Güdel et al. 2007) similar to that of Th 28, and concluded that it originates from both a fast material around the jet axis and a slow, poorly collimated molecular component. Furthermore, Beck et al. (2008) found nearly symmetric H₂ emission orientated perpendicularly to the outflow axis extending up to ~70 au.

Beck & Bary (2019) argued that different mechanisms of H₂ excitation can coexist in young stellar systems. Therefore, we need tools to determine which are responsible or dominant for the observed H₂ emission. In several previous studies, the measured $\nu = 2 - 1 S(1)/\nu = 1 - 0 S(1)$ line ratio has been used to distinguish between shock excitation and nonthermal excitation processes, such as UV pumping and fluorescence (Greene et al. 2010; Beck et al. 2008; Beck & Bary 2019). Typically, non-thermally excited H₂ emission regions have line ratios $\nu = 2 - 1 S(1)/\nu = 1 - 0 S(1)$ of around 0.55 (UV excitation, Black & van Dishoeck 1987), whereas the line ratios arising from shocks are between 0.05 (C-type shocks) and ~0.24 (J-type shocks) (Smith 1995). The spectrum of Th 28 shows that the $\nu = 2 - 1 S(1)$ line is quite faint, and its emission is concentrated on the stellar source. Therefore, our measurement of the ratio is related to this compact spatial region. The pixel-to-pixel ratio of these two lines, dereddened using $A_V = 6$ mag, is ~0.03–0.09 (with uncertainties between 0.007–0.04), which agrees with those found for several classical T Tauri star outflows (Beck et al. 2008). This value is in accordance with C-type shocks.

At the same time, other ratios of H₂ lines can also be used for this goal. For example, the ratio $\nu = 1 - 0 S(1)/\nu = 1 - 0 Q(1)$ (Beck et al. 2008) is well determined in our data at positions away from the driving source, and therefore we can compute the ratio for the faint extended V-shaped emission located in the peripheral region. This ratio is predicted to be ~1 in the case of UV-pumped fluorescent H₂ (Black & van Dishoeck 1987), while the line ratios arising from C- and J-type shocks are 1.29 and 1.59, respectively (Smith 1995; Beck et al. 2008). Our measured pixel-to-pixel values of $\nu = 1 - 0 S(1)/\nu = 1 - 0 Q(1)$, where these lines have $S/N > 3$, vary between a maximum value of 1.23 ± 0.08 and a minimum value at 0.40 ± 0.09 , with a mean value of 0.70 ± 0.08 , which is lower than predicted by shock excitation and even by UV excitation.

The Th 28 H₂ emission can be compared with that resolved around T Tau N, studied by Gustafsson et al. (2008). In some respects, Th 28 is similar to T Tau N, which is also a YSO with spectral type K0, an age of ~1–2 Myr, and a mass of ~1 M_{\odot} . The outer radius of the spatially resolved H₂ disc-like emission is ~100 au, which is greater than $R \sim 50$ au predicted by the models of Nomura & Millar (2005) and Nomura et al. (2007). However, the H₂ emitting region in the Th 28 disc is ~2.5 larger than that of T Tau N (the Th 28 H₂ emitting disc is also ~2.5 larger than its CO-disc measured by ALMA, Louvet et al. 2016). For the H₂ emission in T Tau N, $\nu = 1 - 0 S(1)/\nu = 1 - 0 Q(1) = 0.9$,

which is similar to the case of Th 28. Gustafsson et al. (2008) argue that the most likely scenario of extended T Tau N H₂ emission is a wide-angle wind that impinges on a flared disc. Taking all this into account, this scenario can also be applied to explain the H₂ emission in the arc-shaped component of Th 28. However, in this scenario, shock excitation is expected, but the ratio $\nu = 1 - 0 S(1)/\nu = 1 - 0 Q(1)$ is lower than predicted by shocks for both Th 28 and T Tau N. Gustafsson et al. (2008) also considered the possibility that H₂ emission arises from excitation in the walls of an envelope cavity by an oblique wind, but concluded that this requires an unusually high velocity of the oblique outflow and/or a small opening angle of the cavity. This scenario is also difficult to apply to the Th 28 case for the same reasons.

Another mechanism that can coexist in the H₂ disc is the photoevaporation of the disc by far-UV photons and X-rays (Störzer & Hollenbach 1999; Gustafsson et al. 2008). This energetic radiation will dissociate molecular hydrogen and ionise atomic hydrogen, resulting in a H I–H₂ transition layer, below which the gas is molecular. As a consequence, this will lead to hydrogen recombination lines such as Pa β . Furthermore, this region will show strong emission from [Fe II] 1.257, 1.644 μm , as well as [S II] 6730 Å, in high-density regions. This photoevaporation mechanism may power a collimated disc wind (Gustafsson et al. 2008). In the case of Th 28 the H₂ emission has a bright central core, which coincides spatially with the emission of Pa β and Br γ . The size of the H₂ emission core is similar to that of atomic hydrogen (at 2.122 μm the H₂ core has $FWHM = 0''.38$, while Br γ has $FWHM = 0''.32$). Therefore, we cannot rule out the possibility that we spatially resolve the inner parts of the disc, where this excitation mechanism might dominate. After deconvolution by the PSF, the intrinsic FWHM of the bright H₂ core is derived to be ~0''.2, giving the photoevaporation radius to 18 au (at 185 pc). This radius is three times larger than that determined for T Tau N (~6 au) by Gustafsson et al. (2008). However, according to the models of Dullemond et al. (2007), the radius of the photoevaporation region induced by far-UV radiation can range from 3–150 au for solar-mass stars. The photoevaporative disc wind models calculated by Rab et al. (2022) predict that the majority of H₂ 2.122 μm luminosity will be confined to a radius of 30 au. Therefore, our estimation of the bright H₂ core for Th 28 is within these limits. The wind models of Rab et al. (2022) also show a low maximum radial velocity of the H₂ 2.122 μm line, $|v_p| < 6 \text{ km s}^{-1}$, for a low-inclined circumstellar disc (e.g. Th 28) that in general agrees with our measurements of the H₂ RV.

Shock-excited H₂ emission in YSO jets represents less collimated and more massive molecular outflows with velocities of the order of ~1–30 km s^{-1} , which are believed to consist of shells of ambient gas swept up by the jet bow shock and an ambient slower and wider angle component (Frank et al. 2014). For instance, RW Aur featuring a high collimated jet shows a low-velocity spatially extended arc-shaped H₂ emission (Beck et al. 2008). Observations of the jets of RW Aur and DG Tau (Melnikov et al. 2009; Agra-Amboage et al. 2011) also confirm that the jet gas shows a clear drop in velocity toward the jet edges, which is in contrast to the classical X-wind model, where the ejection speed is similar at all angles (Shang et al. 2007; Frank et al. 2014).

Our 2D SINFONI direct images do not show any elongation of the H₂ emission along the jet. However, the PV diagram of H₂ 2.122 μm (Fig. 10) reveals faint H₂ emission distributed along the jet (this diagram is similar to Fig. 2 from Coffey et al. 2010). PV diagram of another bright H₂ line at 2.407 μm has the same morphology. Therefore, we calculated

the ratio $\nu = 1 - 0 S(1)/\nu = 1 - 0 Q(1)$ from the PV diagrams. We excluded the central part of the emission around the jet source to avoid a contribution from other subsystems. We found $\nu = 1 - 0 S(1)/\nu = 1 - 0 Q(1) = 1.39 \pm 0.34$ between 0''5 and 1''3 in the red lobe and 1.29 ± 0.26 between 0''5 and 1''4, corresponding roughly to the C-type shock ratio (Smith 1995), but the measured ratio errors are quite high in our case. Since this H₂ emission also shows a very low RV, it can arise from a low-velocity ambient gas surrounding the central, higher-velocity lobe. On the other hand, this low H₂ emission can also trace a lower velocity molecular wind surrounding the inner fast jet, as suggested for DG Tau (Agra-Amboage et al. 2014).

Another scenario is that this morphology of the H₂ emitting region is formed by scattering of the emission by a cavity that the jet drilled into the parent circumstellar envelope. This scenario could explain the bright bump in the H₂ emission, which coincides with the shorter blueshifted lobe. Since the measured jet inclination is close to the plane of the sky ($i \sim 80^\circ$), we should see that the circumstellar disc is almost edge-on. YSOs where outflows have swept out most of the mass of the parent cloud can form cavities with biconical morphology, which has been considered for Herbig Ae/Be stars (Fuente et al. 2002). For instance, LkH α 233, which has a biconical nebulosity, has an age of ~ 7 Myr (Hernández et al. 2004).

Th 28 is optically visible despite the high inclination of its circumstellar disc. This, as well as its spectral energy distribution, argues against the presence of a massive envelope with bipolar cavities, similar to those of Class 0 and I objects, for which scattering of line and continuum emission has been observed (e.g. Fedriani 2020). Although a tenuous dusty envelope may be present around Th 28, it should scatter not only H₂ photons but also those of the continuum. To verify its presence, the *K*-band data cube was spectrally collapsed, after subtracting the line emission. This produced a continuum image with an S/N that exceeded that of the integrated H₂ emission image. Comparison with the latter showed that the continuum map has a round and symmetric shape and completely lacks the extended morphology seen in H₂. Thus, we conclude that the structure of the H₂ emission cannot arise from the walls of the outflow cavity or from dust scattering.

Finally, we conclude that the H₂ emission in Th 28 consists of three components: the arc-like extended emission concentrated in the circumstellar disc plane, the bright inner emission centred around the jet source, and the faint bipolar component elongated along the jet lobes. We suggest the following scenarios for the formation of the components. The extended H₂ emission in the disc plane is shock-excited by a wide-angle wind that impinges on the flared disc (Gustafsson et al. 2008). The origin of this wide-angle component is still debated, but its existence is predicted by models (e.g. Cabrit et al. 1999). Takami et al. (2006) describe it as an “unseen wide-angle wind”. Its origin may be the wide-angle molecular wind surrounding the inner fast jet (e.g. Takami et al. 2004). The central bright emission core within $R \sim 18$ au may represent the region in the disk where the photoevaporation mechanism dominates. The faint bipolar H₂ emission probably traces a low-velocity and wide-angle molecular wind surrounding the inner fast and collimated jet.

4.4. Spectroastrometry of emission photocentre

The high-spatial-resolution SINFONI images allowed us to reveal positional shifts of the emission photocentre with respect to the

position of the stellar continuum as a function of wavelength. A shift in the emission peak was detected in bright lines that belong to different gaseous structures. The strongest shift was discovered in the direction of the jet axis, but the [Fe II] and H₂ also reveal an apparent shift in the orthogonal direction, along the disc axis. The lines with the strongest positional shift are the [Fe II] lines, where these shifts reach ~ 30 – 55 au in the redshifted jet lobe. A smaller shift of ~ 13 au was detected in the Br γ line, as well as H₂ 2.413 μm . This value is more than an order of magnitude lower than that measured using the same line for two massive YSOs (Grave & Kumar 2007). This implies that the line displacement may depend on the mass of the central source.

This emission displacement indicates that we probably resolved the region where the jet is forming and that the [Fe II] emission reaches its maximum at a greater distance from the central source. Moreover, the same effect for the H₂ emission, which arises in an orthogonal plane, implies that these processes can also influence the circumstellar gaseous regions. The size of the H₂ positional shift is also smaller than that of [Fe II] and H I, which probably means that the surface where H₂ interacts with the jet is relatively small. However, the molecular hydrogen emission, as well as the [Fe II] emission, shows a shift along the circumstellar disc plane, whereas the atomic hydrogen lines do not reveal this behaviour. Together, these details indicate a complex picture of gas interaction in the compact region where the jet forms.

As in the case of brightness asymmetry, we can also see here a prominent asymmetry in the [Fe II] photocentre shift found near the central source for opposite jet lobes. The largest shift along the jet axis is detected for the (longer) red lobe, whereas for the (shorter) blue lobe the shift is much smaller. The same displacement can also be observed for the Pa β and Br γ lines. One of the possible origins could be an occultation effect from the circumstellar disc, which blocks radiation from the jet lobes close to the jet source. Since the circumstellar extinction in the direction to Th 28 is low (see Sect. 4.1) and the jet axis is close to the sky plane (inclination of 10 – 15°), the occultation effect cannot be responsible for the displacement of 55 au in the [Fe II] 1.644 line. On the other hand, the [Fe II] sequence in Fig. 4 shows that the absolute flux maximum shifts in either the blue or red direction. At the same time, the absolute flux in the red direction is stronger than in the blue direction (Sect. 4.1), which is indicative of a real emission shift (or scattering) rather than an occultation effect. This strongly suggests that the formation of the observed brightness asymmetry of the jet lobes may be linked to a different intensity at the level of the jet formation process (such as different mass loss rates in opposite directions) near the driving source. However, the observations presented here cannot distinguish whether this shift belongs to the circumstellar atomic gas or to the gas component that flows in the jet.

5. Conclusion

SINFONI high-resolution images reveal the clear and simple structure of the highly collimated bipolar jet of Th 28. The [Fe II] emission originates in the highly collimated jet lobes, while the bright H₂ emission arises from an arc-shaped region orthogonal to the jet axis. Our conclusions can be summarised as follows.

1. The arc-like shape of the H₂ emission indicates that the excited H₂ is concentrated in the circumstellar disc and that this excitation can be caused by shocks from a wide-angle stellar wind impinging on the disc, rather than excited by shocks in the jet or fluorescence. The size of the spatially

resolved emission disc, measured from the brightest H₂ line at 2.122 μm, is ≥ 540 au.

2. In addition to the arc-shaped H₂ emission detected directly on the SINFONI images, PV diagrams of the bright H₂ lines reveal faint H₂ emission along both jet lobes, as also reported by Coffey et al. (2010). The H₂ PV diagrams show that the molecular hydrogen emission has a very low velocity compared to forbidden line emission, traced by the [Fe II] lines.
3. The Paβ and Bry lines reveal a two-component morphology. Although the unresolved bright HI emission is concentrated on the central jet source position, there is also a faint extended emission associated with the jet lobes. The line width of this HI emission is about ~ 250 km s⁻¹.
4. The arc-shaped H₂ emission shows a low-velocity pattern. The measured width of the H₂ lines is ≤ 100 km s⁻¹, about 2.5 times less than that of Paβ and Bry.
5. Two gaseous knots visible in [Fe II] are detected in the bipolar jet, one in each lobe, at angular distances of 1'' in the blue lobe and 1''2 in the red lobe.
6. The emission centroid in all gas lines is shifted with respect to the central stellar jet source, which indicates that the observations resolve a region where the inner jet forms. Therefore, the [Fe II] emission displacement traces a change in the excitation of the gas, as the jet propagates in the medium. The HI emission displacement traces the neutral hydrogen that has been entrained by the jet from the accretion region, or the inner hot parts of the jets which is likely to emit in HI lines.
7. The observed extension of the opposing jet lobes, traced by [Fe II] emission, correlates with the value of the [Fe II] photo-centre shifts with respect to the jet source. This suggests that the observed brightness asymmetry is intrinsic and arises in the immediate vicinity of the driving source of Th 28.
8. The maximum size of the jet launch region is derived as 0'015, which corresponds to 3 au, and the initial opening angle of the Th 28 jet is obtained as $\sim 28^\circ$, making this jet substantially less collimated than most of the jets from other CTTs.

Previous NIR 1D spectroscopy of Th 28 jet provided valuable information on the conditions and morphology of the gas in the jet. The results presented in the current study demonstrate that 2D spectroscopy with the SINFONI IFU in the NIR is an effective tool for the study of the gas morphology at high spatial resolution within a 3'' × 3'' field around the central source of Th 28. Spectroscopy of other YSO jets has shown that several optical forbidden doublets ([O I] 6300,6363, [N II] 6548,6583, [S II] 6716,6731 Å) are usually bright in the jet spectrum. Going beyond the present study, we note that 2D spectroscopy of the forbidden line doublets at optical wavelengths with a similarly high spatial resolution would allow us to directly measure basic parameters of the jet in Th 28 in detail, as has been successfully done for several other YSO jets.

Acknowledgements. This work is based on observations obtained with ESO VLT/SINFONI (Paranal, Chile) within the observing programme 095.C-0892(A). We thank the referee for comments that helped to improve the paper. A.C.G. has been supported by PRIN-INAF-MAIN-STREAM 2017 "Protoplanetary disks seen through the eyes of new-generation instruments" and by PRIN-INAF 2019 "Spectroscopically tracing the disk dispersal evolution (STRADE)". RGL acknowledges support from Science Foundation Ireland under Grant No. 18/SIRG/5597. PAB and NSN acknowledge the support of the Russian Science Foundation, grants 18-72-10132 and 21-72-03016, for the initial stages of this project. This research made use of the SIMBAD database, operated at CDS, Strasbourg, France.

References

- Agra-Amboage, V., Dougados, C., Cabrit, S., & Reunanen, J. 2011, *A&A*, **532**, A59
- Agra-Amboage, V., Cabrit, S., Dougados, C., et al. 2014, *A&A*, **564**, A11
- Bacciotti, F., Eisloffel, J., & Ray, T. P. 1999, *A&A*, **350**, 917
- Bai, X.-N. 2017, *ApJ*, **845**, 75
- Bailer-Jones, C. A. L., Rybizki, J., Fouesneau, M., Mantelet, G., & Andrae, R. 2018, *AJ*, **156**, 58
- Bailer-Jones, C. A. L., Rybizki, J., Fouesneau, M., Demleitner, M., & Andrae, R. 2021, *AJ*, **161**, 147
- Bary, J. S., Weintraub, D. A., & Kastner, J. H. 1999, *Am. Astron. Soc. Meeting Abstr.*, **195**, 78.04
- Bary, J. S., Weintraub, D. A., & Kastner, J. H. 2003a, *ApJ*, **586**, 1136
- Bary, J. S., Weintraub, D. A., Kastner, J. H., & Shukla, S. J. 2003b, *Am. Astron. Soc. Meeting Abstr.*, **203**, 147.06
- Beck, T. L., & Bary, J. S. 2019, *ApJ*, **884**, 159
- Beck, T. L., McGregor, P. J., Takami, M., & Pyo, T.-S. 2008, *ApJ*, **676**, 472
- Beck, T. L., Bary, J. S., & McGregor, P. J. 2010, *ApJ*, **722**, 1360
- Beckwith, S., Gatley, I., Matthews, K., & Neugebauer, G. 1978, *ApJ*, **223**, L41
- Béthune, W., Lesur, G., & Ferreira, J. 2017, *A&A*, **600**, A75
- Black, J. H., & van Dishoeck, E. F. 1987, *ApJ*, **322**, 412
- Boley, P. A., Linz, H., Dmitrienko, N., et al. 2019, *A&A*, submitted [arXiv:1912.08510]
- Burton, M. G., Brand, P. W. J. L., Geballe, T. R., & Webster, A. S. 1989, *MNRAS*, **236**, 409
- Cabrit, S., Ferreira, J., & Raga, A. C. 1999, *A&A*, **343**, L61
- Caratti o Garatti, A., Stecklum, B., Linz, H., Garcia Lopez, R., & Sanna, A. 2015, *A&A*, **573**, A82
- Caratti o Garatti, A., Stecklum, B., Weigelt, G., et al. 2016, *A&A*, **589**, L4
- Cardelli, J. A., Clayton, G. C., & Mathis, J. S. 1989, *ApJ*, **345**, 245
- Coffey, D., Bacciotti, F., Woitas, J., Ray, T. P., & Eisloffel, J. 2004, *ApJ*, **604**, 758
- Coffey, D., Bacciotti, F., Podio, L., & Nisini, B. 2010, *ApJ*, **719**, 505
- Comerón, F., & Fernández, M. 2010, *A&A*, **511**, A10
- Davis, C. J., Cervantes, B., Nisini, B., et al. 2011, *A&A*, **528**, A3
- Dougados, C., Cabrit, S., Ferreira, J., et al. 2004, *Ap&SS*, **292**, 643
- Dullemond, C. P., Hollenbach, D., Kamp, I., & D'Alessio, P. 2007, in *Protostars and Planets V*, eds. B. Reipurth, D. Jewitt, & K. Keil, 555
- Dyda, S., Lovelace, R. V. E., Ustyugova, G. V., et al. 2015, *MNRAS*, **450**, 481
- Eisenhauer, F., Abuter, R., Bickert, K., et al. 2003, in *Society of Photo-Optical Instrumentation Engineers (SPIE) Conference Series*, eds. M. Iye, & A. F. M. Moorwood, *Proc. SPIE*, **4841**, 1548
- Elias, J. H. 1980, *ApJ*, **241**, 728
- Fedriani, R., Caratti o Garatti, A., Koutoulaki, M., et al. 2020, *A&A*, **633**, A128
- Ferreira, J. 1997, *A&A*, **319**, 340
- Ferreira, J., & Casse, F. 2004, *ApJ*, **601**, L139
- Ferreira, J., Dougados, C., & Cabrit, S. 2006, *A&A*, **453**, 785
- France, K., Schindhelm, E., Herczeg, G. J., et al. 2012, *ApJ*, **756**, 171
- Frank, A., Gardiner, T. A., Delemarter, G., Lery, T., & Betti, R. 1999, *ApJ*, **524**, 947
- Frank, A., Ray, T. P., Cabrit, S., et al. 2014, in *Protostars and Planets VI*, eds. H. Beuther, R. S. Klessen, C. P. Dullemond, & T. Henning, 451
- Fuente, A., Martín-Pintado, J., Bachiller, R., Rodríguez-Franco, A., & Palla, F. 2002, *A&A*, **387**, 977
- Gaia Collaboration 2018, *VizieR Online Data Catalog*: I/345
- Galli, P. A. B., Bertout, C., Teixeira, R., & Ducourant, C. 2013, *A&A*, **558**, A77
- García Lopez, R., Nisini, B., Giannini, T., et al. 2008, *A&A*, **487**, 1019
- Giannini, T., Calzoletti, L., Nisini, B., et al. 2008, *A&A*, **481**, 123
- Giannini, T., Antonucci, S., Nisini, B., et al. 2015, *ApJ*, **798**, 33
- Gómez, L., Rodríguez, L. F., & Loinard, L. 2013, *Rev. Mex. Astron. Astrofis.*, **49**, 79
- Gondoin, P. 2006, *A&A*, **454**, 595
- Grave, J. M. C., & Kumar, M. S. N. 2007, *A&A*, **462**, L37
- Greene, T. P., Barsony, M., & Weintraub, D. A. 2010, *ApJ*, **725**, 1100
- Güdel, M., Telleschi, A., Audard, M., et al. 2007, *A&A*, **468**, 515
- Gustafsson, M., Labadie, L., Herbst, T. M., & Kasper, M. 2008, *A&A*, **488**, 235
- Hartigan, P., Raymond, J., & Pierson, R. 2004, *ApJ*, **614**, L69
- Hernández, J., Calvet, N., Briceño, C., Hartmann, L., & Berlind, P. 2004, *AJ*, **127**, 1682
- Hirth, G. A., Mundt, R., Solf, J., & Ray, T. P. 1994, *ApJ*, **427**, L99
- Krautter, J. 1986, *A&A*, **161**, 195
- Louvet, F., Dougados, C., Cabrit, S., et al. 2016, *A&A*, **596**, A88
- Matsakos, T., Vlahakis, N., Tsinganos, K., et al. 2012, *A&A*, **545**, A53
- Meliani, Z., Casse, F., & Sauty, C. 2006, *A&A*, **460**, 1
- Melnikov, S. Y., Eisloffel, J., Bacciotti, F., Woitas, J., & Ray, T. P. 2009, *A&A*, **506**, 763
- Modigliani, A., Hummel, W., Abuter, R., et al. 2007, *ArXiv e-prints* [arXiv:astro-ph/0701297]

- Murphy, A., Dougados, C., Whelan, E. T., et al. 2021, *A&A*, **652**, [A119](#)
- Muzerolle, J., Hartmann, L., & Calvet, N. 1998, *AJ*, **116**, [2965](#)
- Natta, A., Testi, L., Muzerolle, J., et al. 2004, *A&A*, **424**, [603](#)
- Nisini, B., Bacciotti, F., Giannini, T., et al. 2005, *A&A*, **441**, [159](#)
- Nomura, H., & Millar, T. J. 2005, *A&A*, **438**, [923](#)
- Nomura, H., Aikawa, Y., Tsujimoto, M., Nakagawa, Y., & Millar, T. J. 2007, *ApJ*, **661**, [334](#)
- Nussbaumer, H., & Storey, P. J. 1988, *A&A*, **200**, [L25](#)
- Podio, L., Bacciotti, F., Nisini, B., et al. 2006, *A&A*, **456**, [189](#)
- Podio, L., Eislöffel, J., Melnikov, S., Hodapp, K. W., & Bacciotti, F. 2011, *A&A*, **527**, [A13](#)
- Pudritz, R. E., Ouyed, R., Fendt, C., & Brandenburg, A. 2007, *Protostars and Planets V*, [277](#)
- Quinet, P., Le Dourneuf, M., & Zeppen, C. J. 1996, *A&AS*, **120**, [361](#)
- Rab, C., Weber, M., Grassi, T., et al. 2022, *A&A*, **668**, [A154](#)
- Ray, T., Dougados, C., Bacciotti, F., Eislöffel, J., & Chrysostomou, A. 2007, in *Protostars and Planets V*, eds. B. Reipurth, D. Jewitt, & K. Keil, [231](#)
- Reipurth, B., Heathcote, S., Morse, J., Hartigan, P., & Bally, J. 2002, *AJ*, **123**, [362](#)
- Shang, H., Li, Z. Y., & Hirano, N. 2007, in *Protostars and Planets V*, eds. B. Reipurth, D. Jewitt, & K. Keil, [261](#)
- Smith, M. D. 1995, *A&A*, **296**, [789](#)
- Smith, N., & Hartigan, P. 2006, *ApJ*, **638**, [1045](#)
- Störzer, H., & Hollenbach, D. 1999, *ApJ*, **515**, [669](#)
- Takami, M., Chrysostomou, A., Ray, T. P., et al. 2004, *A&A*, **416**, [213](#)
- Takami, M., Chrysostomou, A., Ray, T. P., et al. 2006, *ApJ*, **641**, [357](#)
- Tambovtseva, L. V., Grinin, V. P., & Weigelt, G. 2016, *A&A*, **590**, [A97](#)
- Wang, H., & Henning, T. 2009, *AJ*, **138**, [1072](#)
- Wassell, E. J., Grady, C. A., Woodgate, B., Kimble, R. A., & Bruhweiler, F. C. 2006, *ApJ*, **650**, [985](#)
- Whelan, E. T., Ray, T. P., & Davis, C. J. 2004, *A&A*, **417**, [247](#)
- White, M. C., Bicknell, G. V., McGregor, P. J., & Salmeron, R. 2014, *MNRAS*, **442**, [28](#)
- Wilking, B. A., Schwartz, R. D., Mundy, L. G., & Schultz, A. S. B. 1990, *AJ*, **99**, [344](#)
- Woitas, J., Ray, T. P., Bacciotti, F., Davis, C. J., & Eislöffel, J. 2002, *ApJ*, **580**, [336](#)